Bioactive Materials 50 (2025) 30–46

Contents lists available at ScienceDirect

Bioactive Materials

journal homepage: www.keaipublishing.com/en/journals/bioactive-materials

A multifunctional hydrogel loaded with magnesium-doped bioactive glass-induced vesicle clusters enhances diabetic wound healing by promoting intracellular delivery of extracellular vesicles

Zetao Wang [a,b,g,1], Zhipeng Sun [a,b,1], Shuangli Zhu [f], Zhihao Qin [a,b], Xiaohong Yin [f], Yilin Ding [a,b], Huichang Gao [e,*], Xiaodong Cao [a,b,c,d,**]

[a] School of Materials Science and Engineering, South China University of Technology, Guangzhou, 510641, PR China
[b] National Engineering Research Centre for Tissue Restoration and Reconstruction, Guangzhou, 510006, PR China
[c] Guangdong Provincial Key Laboratory of Biomedical Engineering, South China University of Technology, Guangzhou, 510006, PR China
[d] Zhongshan Institute of Modern Industrial Technology of SCUT, Zhongshan, Guangdong, 528437, PR China
[e] School of Medicine, South China University of Technology, Guangzhou, 510006, PR China
[f] Institute of Medical Health, Harbin Institute of Technology Zhengzhou Research Institute, Zhengzhou, 450000, PR China
[g] Centre for Translational Medicine Research & Development, Shenzhen Institutes of Advanced Technology, Chinese Academy of Sciences, Shenzhen, 518055, PR China

ARTICLE INFO

Keywords:
Diabetic wound healing
Extracellular vesicles
Magnesium-doped bioactive glass
Multifunctional hydrogel
Angiogenesis

ABSTRACTS

The treatment of diabetic wounds (DWs) poses a significant medical challenge. Mesenchymal stem cell-derived small extracellular vesicles (sEVs) have demonstrated potential in accelerating healing by delivering growth factors and microRNAs. However, the rapid clearance by the circulatory system limits their concentration and bioavailability within cells. This study employed magnesium-doped bioactive glass (MgBG) to autonomously program sEVs into a vesicle cluster (EPPM), which was subsequently incorporated into a hydrogel to create a comprehensive repair system that enhanced the delivery of both sEVs and MgBG, thereby promoting rapid healing of diabetic wounds. This hydrogel exhibited excellent injectable, self-healing and bioadhesive properties, making it an ideal physical barrier for DWs. In addition, the hydrogels also possessed photoresponsive properties that facilitated their bactericidal activity. The released EPPM significantly increased the intracellular uptake and accumulation of sEVs, with approximately 8.2-fold enhancement in macrophages and 16.7-fold in endothelial cells. The EPPM clusters efficiently induce macrophage M2 polarization, reduce inflammatory responses at the wound site, and recruit cells, thereby promoting angiogenesis and collagen deposition. This integrated repair system provided a new platform for the comprehensive treatment of diabetic wounds.

1. Introduction

Diabetes mellitus, a prevalent metabolic disorder characterized by elevated blood glucose levels, is frequently associated with complications such as diabetic ulcers [1], which pose a significant challenge in current clinical practice. Diabetic wounds (DWs) not only escalate medical costs but can also lead to mortality, garnering increasing attention [2]. The treatment process for DWs includes four consecutive and overlapping phases: hemostasis, inflammation, proliferation, and remodeling [3]. Following wound formation, impaired blood supply and the infiltration of inflammatory mediators initiate a rapid inflammatory response. Hyperglycemia, excessive oxidative stress, recurrent infections, and angiopathy can further exacerbate the inflammatory response. Concurrently, the immune microenvironment undergoes remodeling over time to facilitate the entire repair process [4]. Thus, strategies addressing these critical points represent a promising direction for DWs treatment.

Ample evidence has demonstrated that the timely transition of macrophage phenotypes to M2 can expedite the shift from the inflammatory phase to the proliferative phase, accelerating wound healing [5].

Peer review under the responsibility of editorial board of Bioactive Materials.
* Corresponding author.
** Corresponding author. School of Materials Science and Engineering, South China University of Technology, Guangzhou, 510641, PR China.
E-mail addresses: mchcgao@scut.edu.cn (H. Gao), caoxd@scut.edu.cn (X. Cao).
[1] Zetao Wang and Zhipeng Sun are equally contributed to this work.

https://doi.org/10.1016/j.bioactmat.2025.03.025
Received 7 November 2024; Received in revised form 4 March 2025; Accepted 27 March 2025

Various drugs have been identified as candidates for promoting macrophage polarization. Extracellular vesicles (EVs) are small vesicles secreted by donor cells, characterized by a bilayer membrane structure that encapsulates proteins, mRNAs, miRNAs, and other substances derived from the donor cells. Numerous studies have demonstrated that small extracellular vesicles (sEVs) derived from bone marrow mesenchymal stem cells (BMSCs) can modulate inflammatory responses in peripheral tissues, mitigate oxidative stress, promote peripheral angiogenesis, and enhance extracellular matrix deposition, making them widely utilized in wound repair. However, the current application of sEVs faces significant limitations, including rapid degradation by various biological enzymes in the internal environment and the discrete nature of small-sized sEVs, which hinders their effective deposition. Therefore, it is essential to design a carrier for sEVs that prevents their rapid degradation while promoting their deposition and absorption to enhance their therapeutic efficacy.

In the previous research, our team has conducted extensive surface modification investigations on bioactive glass (BGs). These modifications, particularly involving organic coatings, significantly enhanced the protein adsorption and drug-carrying properties of BGs, optimizing the loading and release of small-sized drugs. Magnesium-doped bioactive glass (MgBG) is rich in active ions like Mg^{2+} and Ca^{2+}, which exhibits good biocompatibility along with excellent immunomodulatory and angiogenic capabilities [6,7]. Studies have shown that Mg^{2+} is taken up by cells and subsequently functions intracellularly to regulate cell recruitment, modulate the expression of inflammation-related genes, and promote angiogenesis [8–10]. Furthermore, MgBG surfaces can be modified to facilitate the loading and sustained release of active substances or drugs through protein adhesion or electrostatic interactions [11]. However, BGs, as active substances, have limited ion solubility and are challenging for cells to internalize, which restricts their biological effects. To address these challenges, we propose the combination of BGs with sEVs. Due to their cell membrane-like properties, sEVs can enhance the internalization of BGs by cells, thereby facilitating the more effective exertion of BGs' biological effects within the cellular environment. Additionally, through specific surface modifications, BGs can adsorb a substantial number of sEVs, significantly enhancing the effective deposition of sEVs and promoting their utilization in somatic cells.

Hydrogel dressings have emerged as a promising platform capable of effectively delivering various elements, including drugs, cells, proteins, or bioactive molecules, playing a crucial role in wound healing and tissue function reconstruction [12]. Leveraging hydrogels' high encapsulation efficiency and controlled release in drug delivery can promote the formation of specific vascular networks and better modulate the immune microenvironment of chronic DWs [13]. Conversely, chronic DWs or ulcers often harbor bacterial and microbial infections, leading to persistent inflammatory responses and biofilm formation over time [14]. Bacterial biofilms in refractory wounds are a major cause of chronic wound deterioration and prolonged healing [15]. Clinically, antibiotic drugs are commonly used to prevent wound infections. Unfortunately, due to the prolonged misuse of antibiotics, chronic wound infections may involve multi-drug-resistant bacteria [16]. Near-infrared (NIR)-induced photothermal therapy has emerged as a broad-spectrum antibacterial method in wound treatment due to its non-invasive nature, lack of resistance, and minimal side effects [17]. PDA modification endows MgBGs with excellent photothermal conversion efficiency, making it an ideal choice for photothermal antibacterial therapy [18].

In this study, we present a novel conceptual design involving the self-assembly programming of sEVs derived from BMSCs on MgBG interfaces modified with PDA and poly-L-lysine (PLL), creating sEVs@PPMB (EPPM) vesicle clusters with extraordinary efficiency in enhancing endocytosis. By combining mild Schiff base reactions with oxidized dextran (OD) and quaternized chitosan (QCS), we developed a multifunctional hydrogel (EPPMO) that achieves rapid healing of diabetic ulcers. This composite dressing enables rapid photothermal bacterial eradication without compromising sEVs activity. During the healing process, the hydrogel slowly releases EPPM. Macrophages and endothelial cells efficiently internalize and accumulate the released EPPM to synergistically modulate immune response. It also promotes an immune-friendly microenvironment for healing. Additionally, it enhances angiogenesis and skin regeneration. This design provides comprehensive treatment throughout the diabetic wound healing process, achieving bacterial eradication, cell recruitment, anti-inflammation, and angiogenesis to enhance the efficacy of diabetic wound healing (see Fig. 1).

2. Results and discussion

2.1. Characterization of PPMO hydrogels

The preparation process of PPMO hydrogel is illustrated in Fig. 2a. Initially, PPMB was synthesized by modifying MgBG with PDA and PLL. Scanning electron microscope (SEM) results indicated that PDA-MgBG and PPMB (PP0.2-MB, and PP0.5-MB) exhibited uniform spherical structures (Fig. S1a). Particle size analysis (Fig. S1b) showed that MgBG had a particle size of 464.9 ± 78.56 nm, and the particle size of PP0.5-MB modified with PDA and PLL was 590.4 ± 144.7 nm, consistent with SEM results. Energy dispersive X-ray spectroscopy (EDX) analysis was conducted to further examine the elemental composition of PPMB (Fig. S1c and Table S1). Compared to MgBG (comprising elements such as O, Mg, Si, P, and Ca), PDA-MgBG showed the appearance of nitrogen (0.13 wt%) after PDA modification, and the nitrogen content in PP 0.2-MB and PP 0.5-MB after further PLL modification increased to 1.28 wt% and 1.89 wt%, respectively. Additionally, zeta potential analysis results (Fig. 2b) indicated that MgBG had a zeta potential of −14.8 ± 12.4 mV.

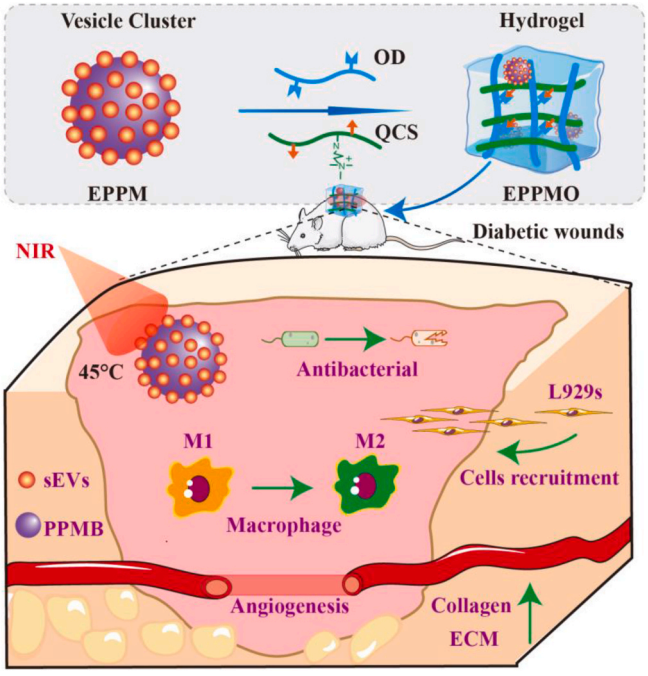

Fig. 1. Schematic diagram of the preparation process of EPPMO hydrogel. EPPM vesicle clusters were mixed with OD and QCS, resulting in the formation of the EPPMO hydrogel. During the healing process of full-thickness skin defects in diabetic infected wounds, the hydrogel initially facilitates photothermal sterilization. The sustained release of EPPM enhances the endocytosis and accumulation of sEVs by macrophages and endothelial cells, thereby improving efficacy and rapidly achieving macrophage M2 polarization. This process leads to angiogenesis, collagen deposition, and accelerated wound healing under immune regulation. PPMB (PDA/PLL-MgBG), EPPM (sEVs/PPMB), L929s (L929 cells), *Escherichia coli* (*E. coli*), and *Staphylococcus aureus* (*S. aureus*) were involved in the study.

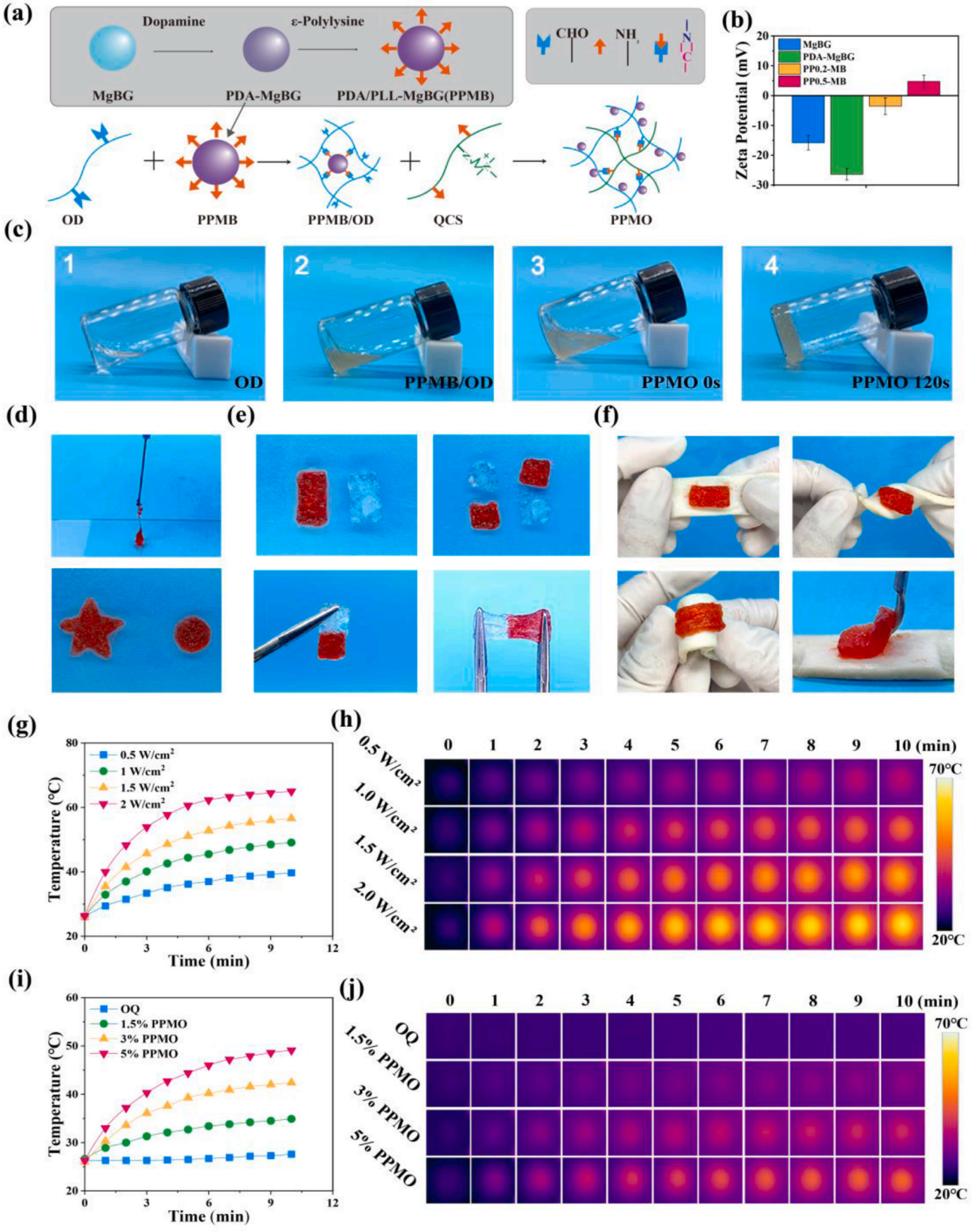

Fig. 2. Characterization of PPMO hydrogel. (a) Schematic illustration of hydrogel preparation. (b) Zeta potential analysis results of nanoparticles presented by SEM. (c) Hydrogel preparation process. (d) Injectability of the hydrogel. (e) Self-healing properties of the hydrogel. (f) Skin adhesion properties of the hydrogel. (g) Temperature variation curves of 5 % PPMO hydrogel (OQ hydrogel loaded with PPMB) at different NIR intensities. (h) Temperature variation images of 5 % PPMO hydrogel at different NIR intensities. (i) Temperature change curve of hydrogel at an NIR intensity of 1 W/cm^2. (j) Temperature change images of hydrogel at an NIR intensity of 1 W/cm^2 * $p < 0.05$, ** $p < 0.01$, *** $p < 0.001$, n = 3.

PDA-MgBG's zeta potential decreased to −26.4 ± 11.0 mV due to PDA oxidation and self-polymerization on the MgBG surface. As the proportion of positively charged PLL increased, the zeta potential of PP0.5-MB rose to 4.75 ± 4.11 mV. X-ray Diffraction (XRD) results (Fig. S1d) showed that the nanoparticles exhibited characteristic bioactive glass peaks (a broad peak around 20–30°) [19], indicating that PDA and PLL modifications did not affect MgBG's crystal structure, maintaining its typical amorphous structure, which suggested good degradation potential. The high PLL content in PP0.5-MB, carrying a positive charge, exhibited potential for adhesion to negatively charged sEVs. Therefore, PP0.5-MB was selected for subsequent experiments.

The chemical structures of OD and QCS were analyzed. The modification process and Fourier Transform Infrared (FTIR) spectroscopy results of OD were shown in Fig. S2a. Compared to dextran, OD exhibited a characteristic aldehyde absorption peak at 1720 cm^{-1}, confirming the successful synthesis of OD. [20]. The modification process and FTIR results of QCS were shown in Fig. S2b. Compared to CS, QCS showed a characteristic quaternary ammonium absorption peak at 1480 cm^{-1}, indicating the successful grafting of glycidyl trimethylammonium chloride (GTMAC) onto chitosan (CS) [21]. These results indicated the successful synthesis of OD and QCS.

The multifunctionality of PPMO hydrogel presents extensive possibilities for various application. The preparation process of PPMO hydrogel was depicted in Fig. 2c. The amino groups on the side chains of PPMB and QCS reacted with the aldehyde groups on the side chains of OD through a Schiff base reaction, with a gelation time of approximately 120 s. The dynamic reversibility of the Schiff base bond endowed PPMO hydrogel with injectability, self-healing, and tissue adhesion properties [21]. The injectability of the hydrogel was demonstrated in Fig. 2d, where it was uniformly extruded through a 1 mL syringe, forming complete star or round shapes. The self-healing properties were shown in Fig. 2e, where two pieces of red and blue PPMO hydrogel contacted and fused into a single entity without an obvious boundary. The injectability of PPMO hydrogel was conducive to dressing retention and wound filling, which provided convenience for clinical surgery. The tissue interface adhesion properties of PPMO hydrogel were shown in Fig. 2f, where the hydrogel adhered to the surface of pig skin, maintaining its form without significant changes after rotation or folding. In addition, the hydrogel also exhibited good cohesiveness, allowing complete peeling, thus minimizing waste residue and the risk of secondary infection.

To quantify the rheological properties of PPMO hydrogel, its shear-thinning behavior was analyzed, as shown in Fig. S2c. The hydrogel's viscosity decreased with increasing shear rate, indicating a progressive breakdown of internal bonds and significant shear-thinning properties. Strain sweep results (Fig. S2d) revealed notable differences in the breaking strain between OQ and 5 % PPMO hydrogel. Additionally, oscillatory strain sweep tests were used to quantify the self-healing behavior of the hydrogel (Fig. S2e). The results showed that the hydrogel transitioned between liquid ($G' < G''$) and solid ($G' > G''$) states over three cycles, demonstrating excellent self-healing performance.

In addition, SEM results showed (Fig. S3) that the nanoparticles were uniformly dispersed in the hydrogel. To assess the interface adhesion performance of the hydrogel, a lap shear test on pig skin was conducted. As shown in Fig. S4a, the maximum tensile strength of OQ was 6.3 ± 1.42 kPa, and 28.2 ± 1.88 kPa for 5 % PPMO (Fig. S4b), indicating an increase in hydrogel interface adhesion tensile strength with higher PPMB content. Enhanced cohesion of the hydrogel facilitated retention in tissues, preventing detachment from the wound due to movement. Additionally, the compressive properties were examined (Fig. S4c). With the addition of PPMB, the compressive strength of the 5 % PPMO hydrogel increased, with maximum pressures of 3.1 ± 1.11 kPa for OQ and 9.7 ± 3.75 kPa for 5 % PPMO hydrogel (Fig. S4d).

The OQ hydrogel, characterized by a pure organic network formed by Schiff base bonds, exhibited softness and deformation sensitivity. Incorporating PPMB into the OQ hydrogel network significantly enhanced the rigidity and toughness of the organic network [22]. The active Schiff base reaction between the organic network and nanoparticles in the PPMO hydrogel facilitated the wrapping of OD molecular chains around PPMB, thereby increasing cohesive energy and mechanical strength. The aldehyde groups on OD primarily facilitated hydrogel adhesion. Adhesion failure might involve internal cohesive failure of the hydrogel or hydrogel-tissue interface failure. The mechanical strength of the OQ hydrogel was weak due to poor cohesion, leading to internal cohesive failure. In PPMO hydrogel, although PPMB addition consumed aldehyde groups, it effectively enhanced hydrogel cohesion, thereby improving tissue interface adhesion. These results demonstrated that we successfully prepared PPMO hydrogel with excellent injectability, self-healing, and tissue adhesion properties, offering convenient application, adaptability, and complete detachment without residue in diabetic ulcer treatment.

Hydrogel dressings with a photothermal effect can generate localized high temperature when excited by near-infrared (NIR) light, effectively disrupting bacterial biofilms [23]. Additionally, eliminating bacteria or biofilms facilitated the bioactivity of sEVs or bioactive metals. The incorporation of PDA-modified PPMB endowed these hydrogels with the ability to convert light energy into heat. This study comprehensively evaluated the photothermal properties of PPMO hydrogels. First, the photothermal effect of 5 % PPMO hydrogel was tested using an 808 nm NIR at different power levels, as shown in Fig. 2g and h. After 10 min of irradiation, the maximum photothermal temperature of 5 % PPMO hydrogel increased from 39.7 °C to 64.3 °C as the NIR intensity gradually increased from 0.5 W/cm^2 to 2 W/cm^2. Notably, at an NIR intensity of 1 W/cm^2, the temperature of 5 % PPMO hydrogel reached 45 °C within 6 min and stabilized. Subsequently, the photothermal performance of hydrogels with varying PPMB content at an NIR intensity of 1 W/cm^2 was assessed, as shown in Fig. 2i and j. Compared with the OQ hydrogel, the maximum photothermal temperature of PPMO hydrogel showed a gradient increase with higher PPMB content, indicating a concentration-dependent relationship. Bacteria, due to their simple cell structure, were highly sensitive to temperature changes, and rapid temperature increases could disrupt their metabolism, leading to cell death [24]. However, temperatures above 50 °C may cause the degradation of miRNA and other active components within sEVs. Therefore, subsequent experiments employed an NIR intensity of 1 W/cm^2, an irradiation time of 6 min, and a target temperature of 45 °C [25]. These results demonstrated that PPMO hydrogel possessed excellent photothermal responsiveness, with the potential to effectively kill bacteria and prevent wound infections in diabetic ulcers.

2.2. Characterization of EPPMO hydrogels

EPPM vesicle clusters were prepared through protein adhesion and electrostatic interaction between sEVs and PPMB, as illustrated in Fig. 3a. Initially, sEVs secreted by BMSCs were extracted using differential centrifugation. TEM and particle size analysis revealed that the sEVs were spherical or saucer-shaped with an average diameter of 63.1 ± 4.12 nm (Fig. 3b and c) [26]. EPPM vesicle clusters were then prepared by co-incubating sEVs and PPMB. Laser scanning confocal microscopy (LSCM) results, shown in Fig. 3d and S5, were used to observe the binding of sEVs to nanoparticles. sEVs were stained green using a cell membrane green fluorescent marker. Compared to unmodified MgBG, the fluorescence intensity of sEVs in PDA-MgBG, PP0.2-MB, and PP0.5-MB was significantly higher. sEVs were uniformly adsorbed onto the MgBG surface, and with an increasing sEVs loading rate, the green fluorescence intensity gradually increased. The sEVs loading rate of the nanoparticles was further quantified, with results shown in Fig. 3e. The sEVs loading rate for untreated MgBG was 4.4 ± 0.40 %, while PDA-MgBG, modified only with PDA, showed some loading capability. The loading rate of PP0.5-MB, modified with both PDA and PLL, was 66.5 ± 0.46 %, significantly higher than other nanoparticles. Additionally, the particle size of EPPM prepared with PP0.5-MB and sEVs was

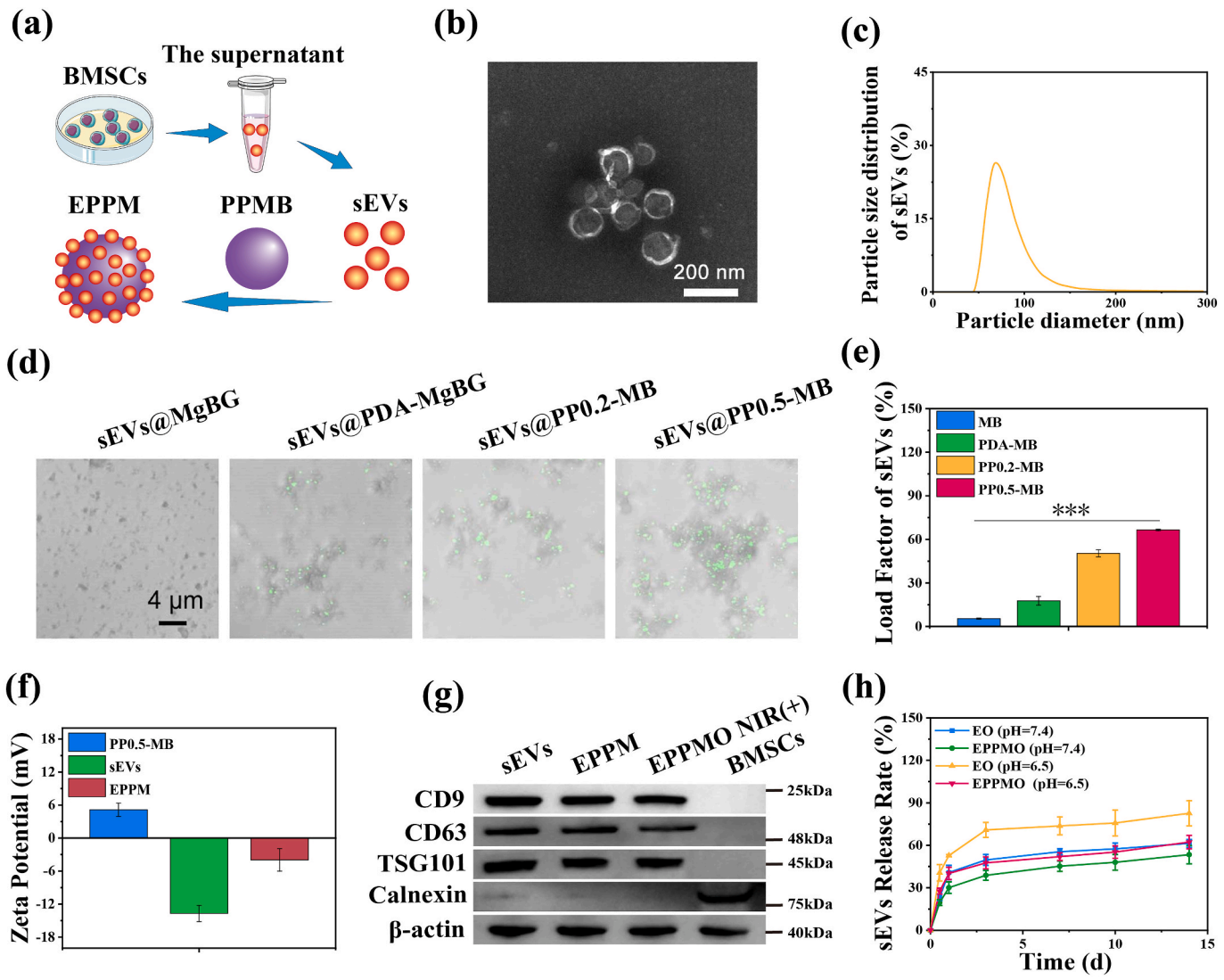

Fig. 3. Characterization of EPPMO hydrogel. (a) Schematic diagram of EPPM preparation. (b) TEM images of sEVs. (c) Nanoparticle size distribution of sEVs. (d) Fluorescent images of composite nanoparticles: sEVs (green) and PPMB (gray). (e) Loading efficiency of sEVs. (f) Zeta potential analysis. (g) Western blot results of extracellular vesicles. (h) Cumulative release results of sEVs from the hydrogel at pH 7.4 and 6.5. * $p < 0.05$, ** $p < 0.01$, *** $p < 0.001$, n = 3.

693.8 ± 84.65 nm (Fig. S6a), larger than that of sEVs and PP0.5-MB alone, due to sEVs adsorbing onto the PP0.5-MB surface. Furthermore, to verify the binding mode between sEVs and PP0.5-MB, zeta potential analysis results were shown in Fig. 3f. PP0.5-MB, positively charged, combined with negatively charged sEVs, resulting in the zeta potential of EPPM vesicle clusters lying between the two, indicating sEVs loading via PDA-mediated protein adhesion and electrostatic interaction.

Maintaining the activity of sEVs is beneficial for their role in tissue regeneration with tissue engineering. To analyze the impact of various treatments on sEVs protein activity, WB results were shown in Fig. 3g. Compared to sEVs, the relative protein levels of CD9, CD63, and TSG101 in sEVs loaded on EPPM and treated with EPPMO NIR (+) decreased by approximately 10 % (Fig. S6b) [26], with no significant difference observed between EPPM loading and EPPMO NIR (+) treatments. Calnexin protein was negative in all components, indicating no endoplasmic reticulum contamination in the extracted sEVs. These results demonstrated that the PPMB loading and 45 °C treatment method have minimal effect on sEVs protein activity, and the sEVs in the EPPMO prepared through a series of treatments retain excellent biological function.

Diabetic ulcers often present a mildly acidic environment due to inflammation [27]. The Schiff base network endowed the hydrogel with pH-responsive sEVs release under mildly acidic conditions [28]. The pH-responsive release results of the hydrogel were shown in Fig. 3h. When sEVs were directly loaded onto OQ hydrogel, the EO hydrogel released rapidly within 3 d and reached equilibrium, with a release rate of approximately 70.8 % at pH = 6.5. In contrast, EPPMO hydrogel released only 47.5 % of sEVs at pH = 6.5 within 3 d. This difference arised from the different loading methods of EO and EPPMO. The sEVs within EO are released responsively through Schiff base cleavage under mildly acidic conditions, causing hydrogel network destruction. In EPPMO hydrogel, sEVs were anchored onto PPMB, tightly cross-linked by the Schiff base network, achieving sustained sEVs release and preventing burst release. The treatment cycle for DWs is generally longer [29]. The long-term sustained release of sEVs from pH-responsive EPPMO hydrogel could effectively prolong the action time of sEVs at the wound site, thereby promoting wound healing.

The cytological activity of EPPMO hydrogels was assessed by utilizing a Transwell co-culture system, as shown in Fig. 4a. Cells were seeded at the bottom of the wells, and 50 μL of hydrogel was placed in the Transwell upper chamber for subsequent cell experiments. The prepared hydrogels exhibited uniform nanoparticle distribution as observed through 3D imaging (Fig. 4b–S7a-b). The results confirmed that sEVs (red), PPMB (green), and EPPM were uniformly distributed

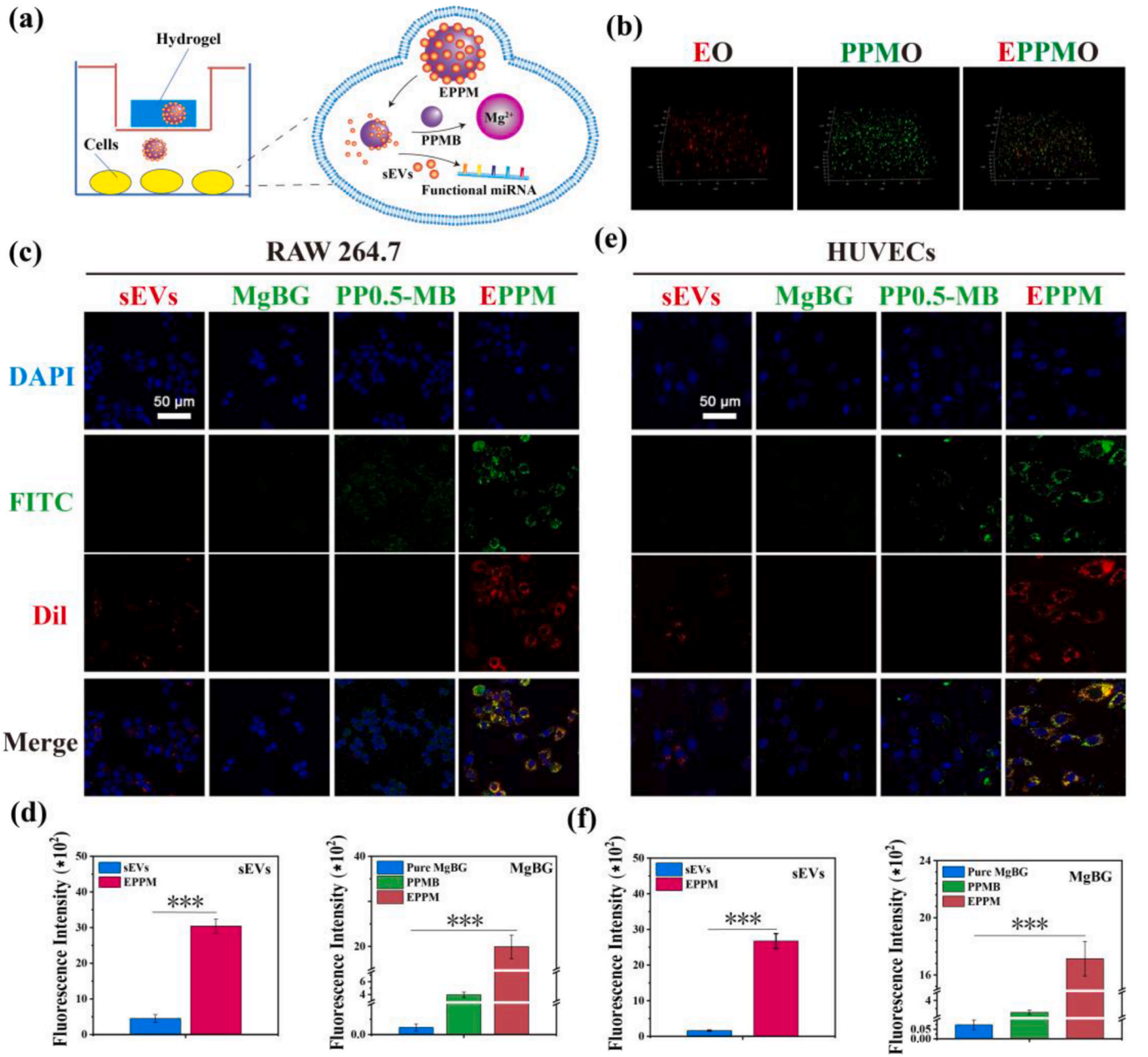

Fig. 4. Detection of cellular internalization of EPPM vesicle clusters. (a) A schematic diagram illustrating the co-culture of cells with EPPMO hydrogel. (b) A 3D image showing the distribution of nanoparticles within the hydrogel: sEVs (red) and PPMB (green). (c) Results demonstrating the internalization of hydrogel-released nanoparticles by RAW 264.7 cells: sEVs (red), MgBG (green), and PP0.5-MB (green). (d) Quantitative fluorescence area results for sEVs and MgBG internalized by RAW 264.7 cells. (e) Results indicating the internalization of hydrogel-released nanoparticles by HUVECs: sEVs (red), MgBG (green), and PP0.5-MB (green). (f) Quantitative fluorescence area results for sEVs and MgBG internalized by HUVECs. * $p < 0.05$, ** $p < 0.01$, *** $p < 0.001$, n = 3. EO (OQ hydrogel loaded with sEVs); PPMO (OQ hydrogel loaded with PPMB); EPPMO (OQ hydrogel loaded with EPPM vesicle clusters); sEVs (sEVs released from EO hydrogel); Pure MgBG (Pure MgBG released from MgBG/OQ hydrogel); PP0.5-MB (PP0.5-MB released from PPMO hydrogel); EPPM (EPPM released from EPPMO hydrogel).

within the hydrogel, demonstrating successful nanoparticle loading using this method. Persistent inflammation is a major challenge in the healing of DWs, making immunoregulation and anti-inflammatory action essential for DWs repair [30]. Macrophages play a key role in anti-inflammatory responses at skin wound sites. The internalization of vesicle clusters by RAW 264.7 cells was analyzed (Fig. 4c). At 12 h, no significant green fluorescence was observed in the unmodified MgBG group, whereas PPMB was internalized by cells but with low fluorescence intensity. Compared to freely released sEVs, the internalization of EPPM by cells increased approximately 8.2-fold (Fig. 4d).

During the proliferation phase of DWs, vascularization is crucial for nutrient transport and wound healing [31]. Human umbilical vein endothelial cells (HUVECs), which are key players in angiogenesis, were examined for vesicle cluster internalization (Fig. 4e). The fluorescence imaging of nanoparticle uptake by HUVECs mirrored that of RAW 264.7 cells, with EPPM showing significantly higher cellular internalization, approximately 16.7-fold compared to sEVs alone (Fig. 4f). Although sEVs released from EO hydrogels could be captured and internalized by cells, their dispersed free state results in lower efficiency. Unmodified MgBG, as the inorganic nanoparticle, has limited cell capture ability. Despite PDA and PLL modifications enhancing MgBG intracellular delivery, it lacks the complexity of biological systems [32]. EPPM vesicle clusters, formed by self-assembly of sEVs on the PPMB interface, leveraged the cell membrane structure of sEVs to facilitate cellular uptake.

Macrophages exhibited higher phagocytic activity compared to endothelial cells, leading to different levels of enhancement in EPPMO vesicle clusters in each cell type. Unlike conventional strategies using sEVs as drug carriers for ultra-small nanoparticles, larger nanoparticles like MgBG require cell membrane wrapping for intracellular delivery, despite these membranes lacking bioactivity [33]. Loading vesicle clusters into EPPMO hydrogels preserved sEVs activity, enhanced bioavailability, and promoted MgBG intracellular delivery and accumulation, effectively regulating cellular biological functions.

2.3. Antibacterial performance of hydrogel

In the high-glucose environment of DWs, bacteria such as *E. coli* and *S. aureus* readily proliferate, forming biofilms that impede the efficacy of antibacterial agents [34]. Furthermore, bacterial infections induce chronic inflammation, further hindering wound healing. The antibacterial rate of the hydrogel against the Gram-negative bacterium *E. coli* was shown in Fig. 5a. Under NIR (−) conditions, all OQ hydrogels achieved an over 90 % antibacterial rate against *E. coli*. Under NIR (+) conditions, the photothermal properties of PPMO and EPPMO hydrogels achieved an antibacterial rate of approximately 99.9 %. The colony count results on agar plates (Fig. 5b) were consistent with the absorbance-based antibacterial results, showing no significant colonies for NIR (+) PPMO and EPPMO hydrogels. In addition, the antibacterial rate of the EPPMO hydrogel against the Gram-positive bacterium *S. aureus* was also presented in Fig. 5c. All hydrogels exhibited an over 95 % antibacterial rate against *S. aureus* under both NIR (−) and NIR (+) conditions. The agar plate results (Fig. 5d) corroborated this, showing no significant colonies for NIR (+) PPMO and EPPMO hydrogels. The superior antibacterial ability of PPMO and EPPMO hydrogels under NIR conditions could be attributed to the strong positive charge of QCS within the hydrogel, which disrupted bacterial membranes [16]. Moreover, bacteria are sensitive to temperature changes, and the photothermal properties of the hydrogel rapidly altered the environmental temperature, disrupting bacterial metabolism and leading to cell death [35]. These results demonstrated that the photothermal effect of the EPPMO hydrogel system could effectively disrupt bacterial biofilms, enhance the efficacy of antibacterial agents, and promote diabetic wound healing.

2.4. Biocompatibility and cell recruitment performance of hydrogels

The biocompatibility of the hydrogels with L929s and HUVECs was assessed using CCK8 and Live/Dead cell staining. Hydrogels containing sEVs, specifically EO and EPPMO, have not only shown excellent biocompatibility but also significantly promoted cell proliferation (Fig. 6a–d). This enhancement was attributed to the various nutrients required for cell proliferation carried by sEVs. Furthermore, the results of hemocompatibility test for the hydrogels were presented in Fig. S8, which demonstrated that the hemolysis rate of all hydrogels remained below 5 %, confirming their good blood compatibility.

Recruitment of L929s effectively promoted the regeneration of skin defects. To evaluate the cell recruitment capability of the hydrogels, a 12 h Transwell assay and its quantitative analysis were conducted (Fig. 6e and f). The Control and OQ groups did not exhibit cell recruitment capabilities. However, with the addition of active substances such as sEVs and MgBG, the EO, PPMO, and EPPMO hydrogels significantly recruited L929s, with EPPMO hydrogel showing the most pronounced recruitment capability. Furthermore, a scratch assay was used to assess the hydrogels' ability to promote L929s migration (Fig. 6g). At 24 h, the semi-quantitative analysis of the scratch assay (Fig. 6h) indicated that the migration rate of the Control group was 46.1 ± 10.96 %, whereas the

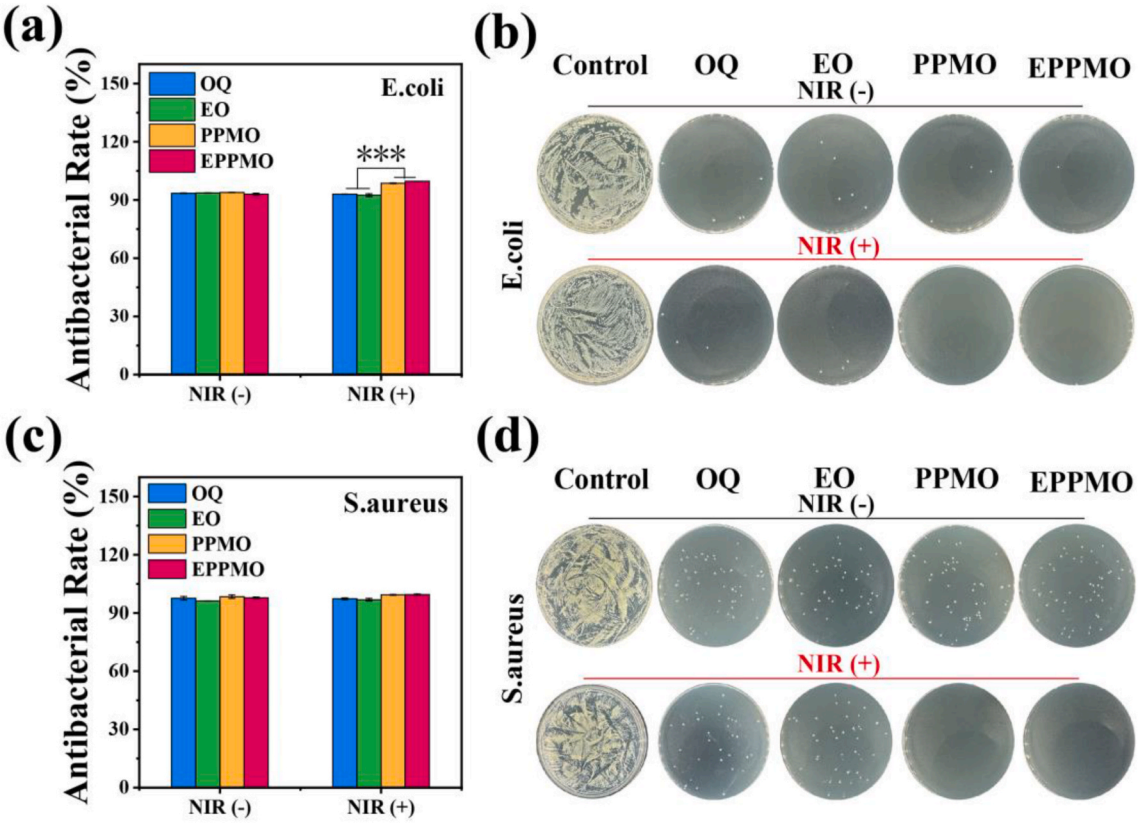

Fig. 5. Photothermal antimicrobial results at 808 nm NIR (1 W/cm^2) of hydrogels. (a) Antimicrobial rate of hydrogel against *E. coli*. (b) Colonies of *E. coli*. (c) Antimicrobial rate of hydrogel against *S. aureus*. (d) Colonies of *S. aureus*. NIR (−) indicated no NIR treatment, NIR (+) indicated NIR treatment. * $p < 0.05$, ** $p < 0.01$, *** $p < 0.001$, n = 6.

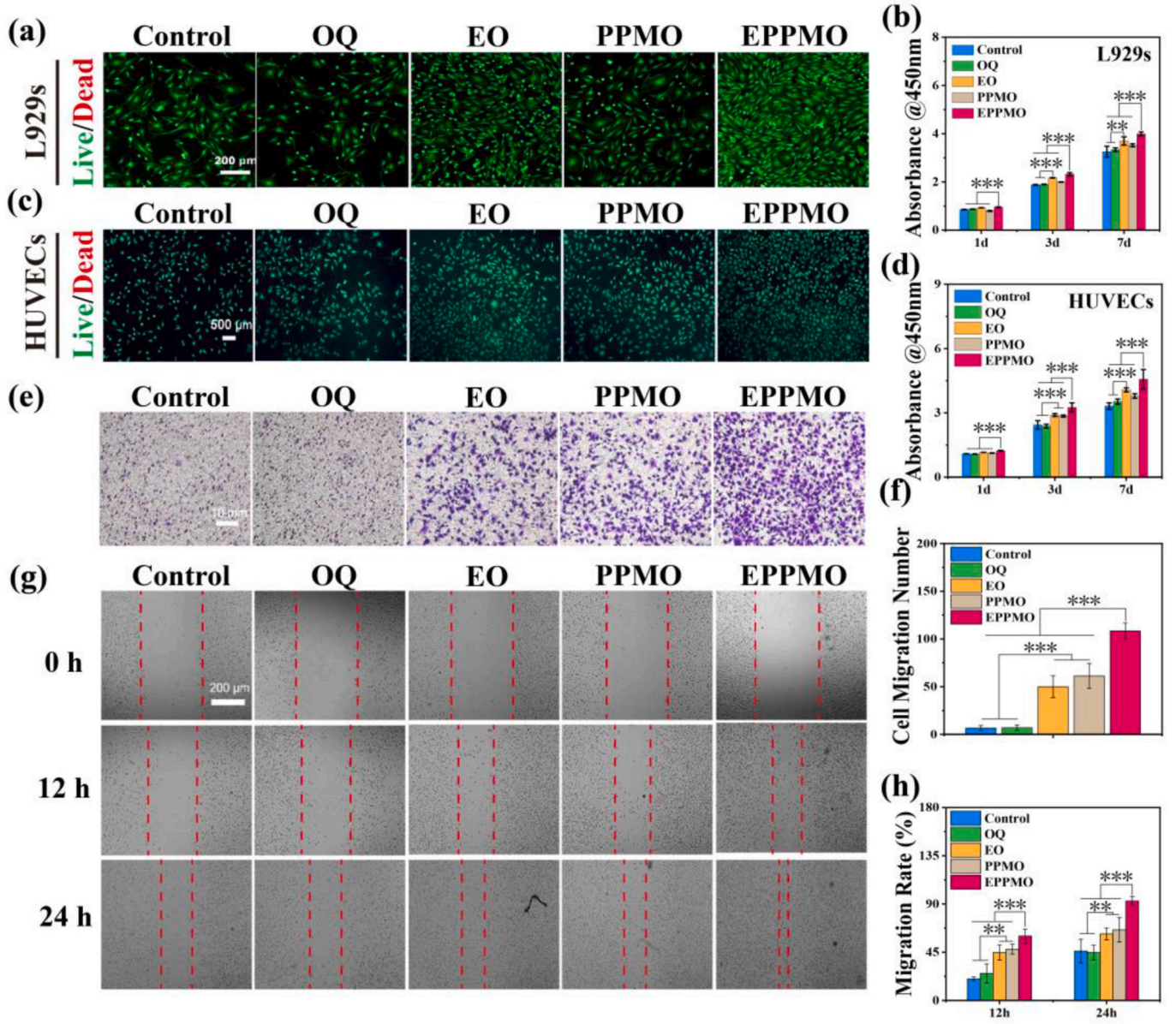

Fig. 6. Biocompatibility and cell recruitment performance of hydrogels. (a) Live/Dead cell staining of L929s with hydrogels. (b) CCK8 assay results for L929s treated with hydrogels. (c) Live/Dead cell staining of HUVECs with hydrogels. (d) CCK8 assay results for HUVECs treated with hydrogels. (e–f) Transwell assay and its semi-quantitative results for L929s with hydrogels. (g–h) Scratch assay and its semi-quantitative results for L929s with hydrogels. $^{*}p < 0.05$, $^{**}p < 0.01$, $^{***}p < 0.001$, n = 3.

EPPMO hydrogel group achieved a migration rate of 92.7 ± 4.07 %. The scratch area had completely disappeared in the EPPMO hydrogel group compared to other groups. This effect was attributed to the synergistic action of sEVs and MgBG. The sEVs, functioning as cell communication tools, carry various active factors, such as SDF-1, which recruit cells [36]. Concurrently, MgBG releases active ions like Mg^{2+}, promoting cell recruitment and migration to the wound site, thereby accelerating tissue regeneration [9]. These results demonstrated that EPPMO hydrogels possessed excellent biocompatibility and could promote cell proliferation, recruitment, and migration, thereby facilitating wound healing.

2.5. M2 phenotype polarization of macrophages

The excessive proportion and persistent presence of M1 phenotype macrophages in DWs significantly impede wound healing [30]. The polarization of macrophages to M2 phenotype can promote the healing of diabetic wounds by secreting a large number of anti-inflammatory factors [9]. Initially, Real-time quantitative reverse transcription PCR (RT-qPCR) was used to assess the expression of inflammation-related genes in RAW 264.7 cells, as shown in Fig. 7a. Lipopolysaccharide (LPS) polarized M0 macrophages to the pro-inflammatory M1 type, resulting in elevated expression of M1 markers TNF-α and iNOS, and decreased expression of anti-inflammatory M2 markers Arg-1 and IL-10 compared to the untreated control group [37]. The OQ hydrogel group showed no significant difference in TNF-α and iNOS expression compared to the LPS group. However, with the inclusion of sEVs and MgBGs, the EO hydrogel, PPMO hydrogel, and EPPMO hydrogel groups demonstrated reduced expression of TNF-α and iNOS and significantly increased expression of M2 markers Arg-1 and IL-10, especially IL-10. Immunofluorescence staining was also used to detect the expression of M1 macrophage marker iNOS and M2 macrophage marker IL-10. The results indicated that iNOS expression was significantly lower in the EPPMO hydrogel group compared to the control group, LPS group, and OQ group (Fig. 7b and c). Conversely, IL-10 expression was significantly

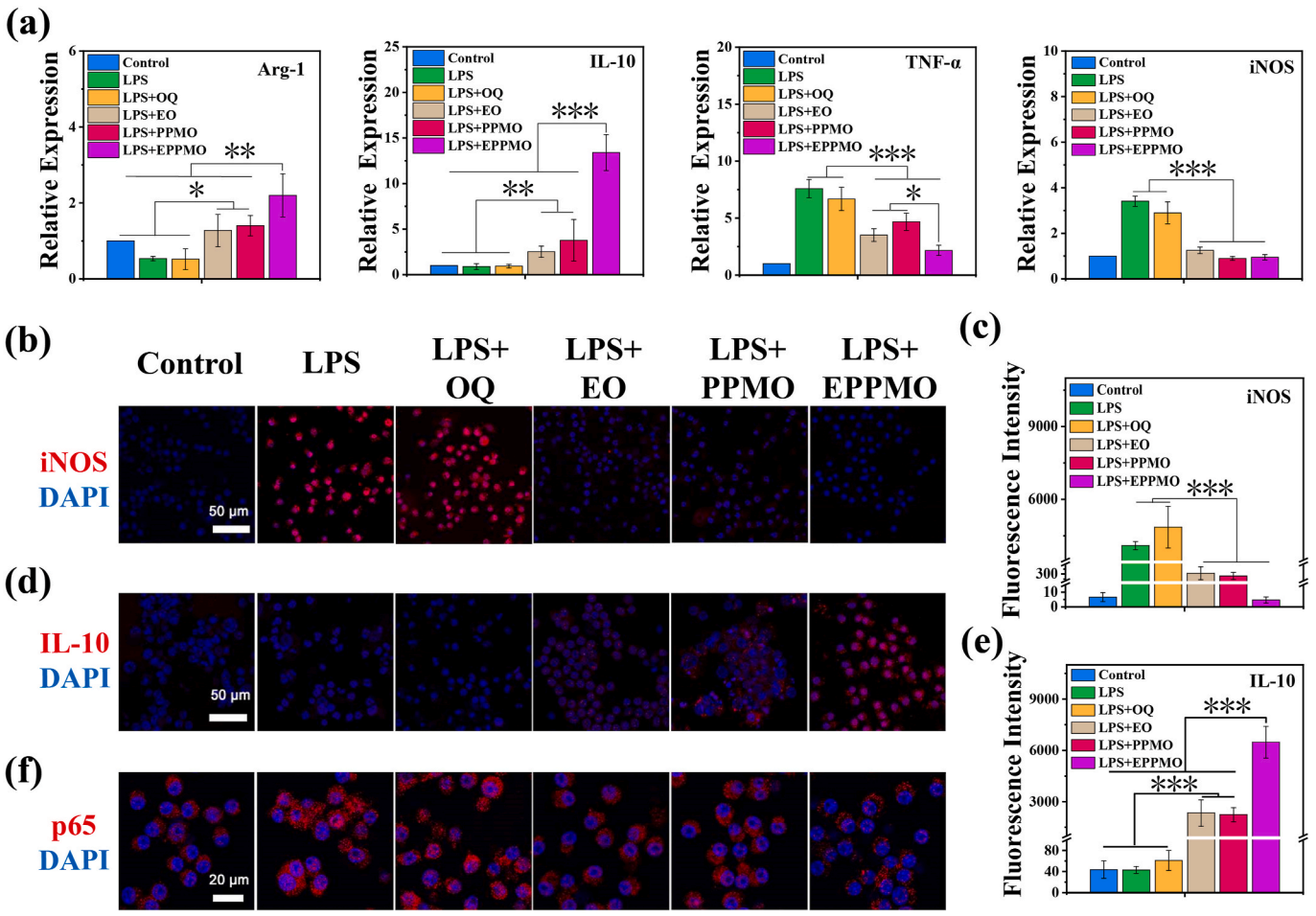

Fig. 7. Hydrogel's ability to modulate macrophage polarization. (a) The expression of anti-inflammatory genes Arg-1 and IL-10, and pro-inflammatory genes TNF-α and iNOS in macrophages detected by RT-qPCR. (b–c) Immunofluorescence staining and semi-quantitative analysis of iNOS protein expression. (d–e) Immunofluorescence staining and semi-quantitative analysis of IL-10 protein expression. (f) Immunofluorescence staining of p65 protein. * $p < 0.05$, ** $p < 0.01$, *** $p < 0.001$, n = 3.

higher in the EPPMO hydrogel group (Fig. 7d and e). Additionally, immunofluorescence staining of the p65 protein in the NF kappa B (NF-κB) signaling pathway was conducted (Fig. 7f) [38]. In the inactive state of the NF-κB signaling pathway, the p65 protein (red) remained in the cytoplasm with inhibited nuclear translocation (control group). LPS-treated macrophages exhibited NF-κB pathway activation, polarizing to M1 macrophages with p65 translocation to the nucleus (LPS group and OQ group). The EPPMO hydrogel group showed the most significant inhibition of p65 nuclear translocation compared to other groups, which attributed to the effective endocytosis of EPPM released from the EPPMO hydrogel. EPPM within cells carried miR-199a, miR-146 [39], and other immunomodulatory miRNAs, and MgBG released Mg^{2+} [40], whose synergistic action with miRNAs effectively inhibited NF-κB pathway activation, thereby preventing p65 nuclear translocation and promoting M1 to M2 macrophage polarization, achieving a combined anti-inflammatory effect.

2.6. Angiogenesis

During the proliferation phase of DWs, vascularization facilitates nutrient transport and promotes wound healing [41]. In this work, RT-qPCR was used to detect the expression of angiogenesis-related genes in HUVECs, as shown in Fig. 8a–d. The OQ hydrogel group showed no significant difference in angiogenesis-related gene expression compared to the Control group. The EPPMO hydrogel group exhibited a significant upregulation of HIF-α and VEGF gene expression, particularly VEGF, compared to the EO hydrogel and PPMO hydrogel groups. Additionally, the VEGF receptor KDR was significantly upregulated. eNOS, which promotes angiogenesis, also showed a marked upregulation in the EPPMO hydrogel group.

To further assess the angiogenic performance of the hydrogels on HUVECs, immunofluorescence was employed to detect the expression of the angiogenesis marker protein CD31 [42]. As illustrated in Fig. 8e and f, the OQ hydrogel group and the Control group showed no significant positive expression of CD31 (red). In contrast, the EO, PPMO, and EPPMO hydrogel groups demonstrated an ability to promote CD31 expression, with the EPPMO hydrogel group showing the most significant increase. This effect was based on the synergistic action of sEVs and MgBG. The combination of sEVs and MgBG enhanced cellular internalization, thereby exerting efficient pro-angiogenic capabilities. Once internalized, sEVs released pro-angiogenic miRNAs (e.g., miR-146a), while MgBG released Mg^{2+}, which regulated angiogenesis [43,44]. Together, these factors synergistically promoted the expression of angiogenesis-related genes, aiding the restoration of the vascular network at the wound site. In addition, matrix gel-forming tube test was also performed, and the results were showed in Fig. 8g, indicating a similar trend to immunofluorescence staining. These findings indicated that the EPPMO hydrogel promoted angiogenesis during diabetic wound healing, facilitating subsequent nutrient transport and accelerating wound healing.

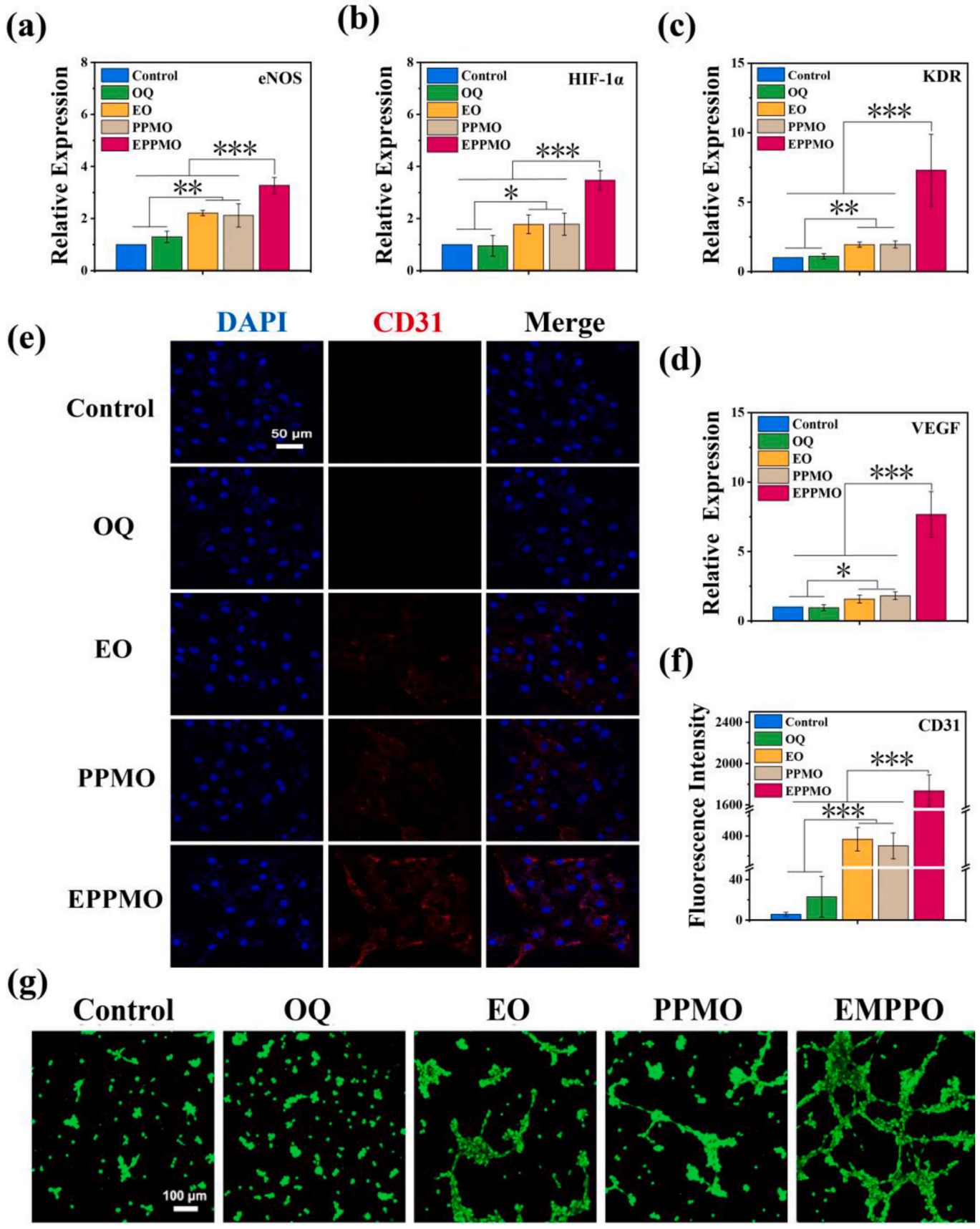

Fig. 8. Evaluation of hydrogel angiogenesis performance. (a–d) The expression of angiogenesis-related genes HIF-α, VEGF, KDR, and eNOS in HUVECs detected by RT-qPCR. (e–f) Immunofluorescence to measure the expression of the CD31 (red) protein and its semi-quantitative analysis results. (g) Calcein AM staining of matrigel matrix-forming vessels. * $p < 0.05$, ** $p < 0.01$, *** $p < 0.001$, n = 3.

2.7. Animal experiments

To validate the in vivo pro-wound healing properties of the hydrogels, a full-thickness skin defect model of diabetic infected wounds in Sprague-Dawley (SD) rats was utilized (Fig. 9a) [45,46]. After 3 d, the wounds in the Blank group had not scabbed and were festering (Fig. 9b), while the OQ and EO hydrogel groups showed no significant festering. In addition, the wounds in the PPMO and EPPMO groups crusted rapidly without obvious signs of infection and ulceration due to the mild photothermal effect of the nanoclusters and the antimicrobial properties of QCS. It is noteworthy that the wounds of the EPPMO group showed initial signs of healing. After 14 d, the EPPMO group had almost completely healed, and other hydrogel groups exhibited good healing, whereas the Blank group had not fully scabbed. Semi-quantitative analysis of tissue morphology (Fig. 9c and d) indicated that the wound healing rate in the EPPMO hydrogel group was significantly higher than other groups. Hematoxylin and Eosin (H&E) staining was also employed to further analyze the morphologic characteristics of the neogranulation tissue to assess the therapeutic efficacy of the hydrogel (Fig. S9). At 3 d, the Blank group showed no significant ECM deposition. Compared to the EO and PPMO hydrogel groups, the EPPMO hydrogel group had begun to show significant ECM deposition. At 7 d, although the EO and PPMO hydrogel groups exhibited significant ECM deposition, the EPPMO hydrogel group showed a more pronounced increase in ECM, with higher deposition density. At 14 d, all hydrogel groups had exhibited epithelialization of the wounds. However, the ECM in the Blank and OQ groups were loosely oriented and lacked direction. In contrast, the ECM deposition in the EO, PPMO, and EPPMO hydrogel groups, which contain active substances, was denser and well-oriented. Notably, the EPPMO hydrogel group showed evident skin appendages such as hair follicles and sebaceous glands, indicating high-quality skin healing. This superior healing was attributed to the slow release of the EPPM clusters during the wound remodeling phase. EPPM clusters were internalized more efficiently by the cells, resulting in increased bioavailability and promoting high quality skin repair.

Prolonged inflammatory response is a well-known characteristic of DWs [41,47]. As described previously, EPPMO Hydrogel alleviated excessive inflammatory response and promoted neoangiogenesis at the wound site through antimicrobial properties and the release of EPPM clusters. To further investigate the inflammatory microenvironment and angiogenesis in SD rats, immunohistochemical staining of wound tissues for the anti-inflammatory marker IL-10 (green, Fig. 10a,d) and the

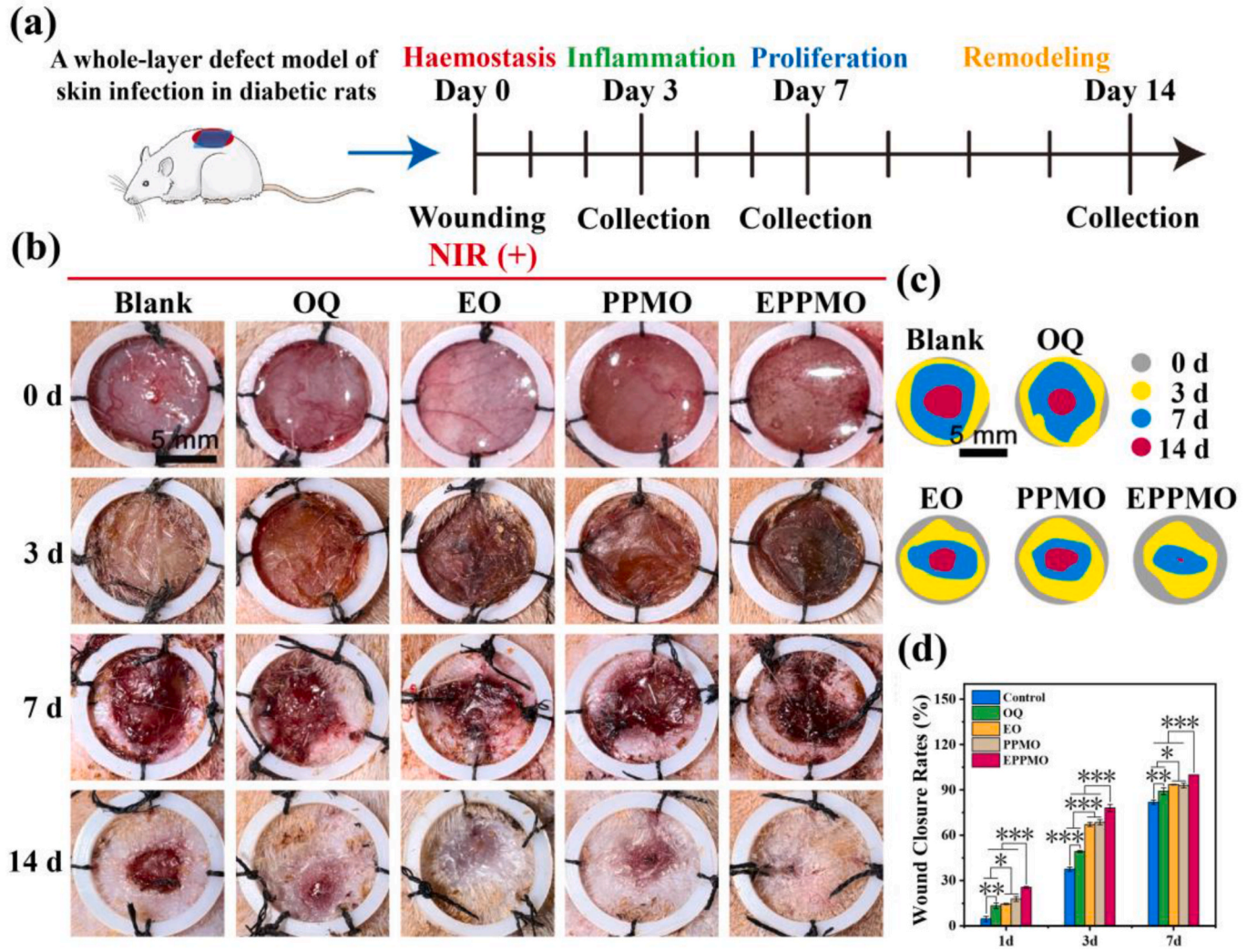

Fig. 9. Evaluation of the effect of hydrogel system combined with near-infrared radiation on promoting the healing of diabetic skin defects. (a) Schematic diagram of the construction process of Diabetic skin wound model. (b) Macroscopic images of skin wound areas treated with different hydrogel samples. (c) Schematic diagrams of skin wound closure for the five groups on postoperative days 3, 7, and 14. (d) Quantitative data on the wound closure rates for the five groups on postoperative days 3, 7, and 14. * $p < 0.05$, ** $p < 0.01$, *** $p < 0.001$, n = 6. Groups are categorized as Blank (untreated control group); OQ (plain hydrogel group); EO (OQ hydrogel loaded with sEVs); PPMO (OQ hydrogel loaded with PPMB); and EPPMO (OQ hydrogel loaded with EPPM vesicle clusters).

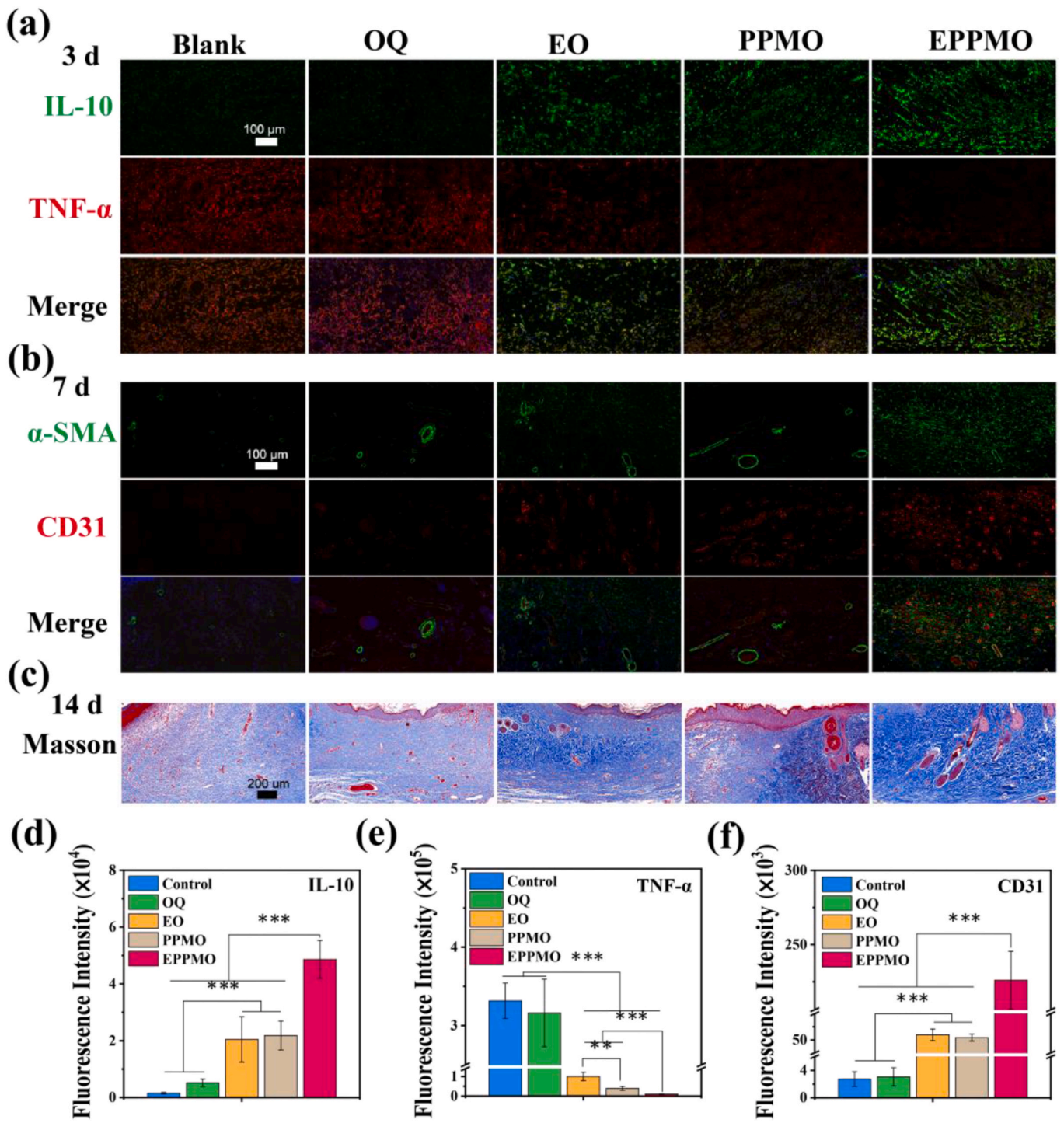

Fig. 10. Histological Immunofluorescence and Masson Staining. (a) Immunofluorescence staining for IL-10 (green) and TNF-α (red). (b) Immunohistochemical staining for α-SMA (green) and CD31 (red). (c) Masson staining. (d) Semi-quantitative results of the fluorescent area for IL-10 immunofluorescence staining. (e) Semi-quantitative results of the fluorescent area for TNF-α immunofluorescence staining. (f) Semi-quantitative results of the fluorescent area for CD31 immunofluorescence staining. * $p < 0.05$, ** $p < 0.01$, *** $p < 0.001$, n = 6. Blank (untreated control group); OQ (pure hydrogel group); EO (OQ hydrogel loaded with sEVs group); PPMO (OQ hydrogel loaded with PPMB group); EPPMO (OQ hydrogel loaded with EPPM vesicle cluster group).

pro-inflammatory marker TNF-α (red, Fig. 10a,e) was conducted. At day 3, the Blank and OQ groups showed significant positive expression of TNF-α, with negative expression of IL-10. However, with the addition of anti-inflammatory agents, the EO and PPMO groups exhibited a significant reduction in pro-inflammatory factors and positive expression of the anti-inflammatory factor IL-10. Under the synergistic effects of sEVs and PPMB, the EPPMO group showed a significant decrease in pro-inflammatory factors and positive IL-10 expression, indicating superior anti-inflammatory capability. Angiogenesis is essential for wound healing, providing oxygen and nutrients to cells involved in the healing process and supporting tissue regeneration. Immunohistochemical staining for α-SMA (green) and CD31 (red) was used to evaluate angiogenesis in DWs (Fig. 10b,f). The Blank and OQ groups showed low CD31 expression, while the PPMO group with incorporated sEVs

increased the expression of the related protein. The EPPMO group, benefiting from the synergistic action of sEVs and PPMO, showed significantly enhanced expression. Angiogenesis aids in maintaining cellular metabolism and proliferation, thus promoting diabetic wound healing.

Masson staining was employed to analyze collagen deposition for skin repair, as shown in Fig. 10c and S10. At 3 and 7 d, the Blank group exhibited only a small amount of collagen expression (blue). Collagen deposition had already begun in the EO and PPMO hydrogel groups, while the EPPMO hydrogel showed significant collagen deposition. At 14 d, collagen expression was evident in both the Blank and OQ groups, with more pronounced collagen expression in the EO, PPMO, and EPPMO hydrogels containing active substances. Notably, collagen in the EPPMO group was densely arranged and mature.

Currently, hydrogel dressings based on sEVs or MgBG have been widely used to promote diabetic wound healing due to their excellent anti-inflammatory, antibacterial, and pro-angiogenic properties. However, most previous studies have focused primarily on the sustained release of sEVs and MgBG from the dressings, neglecting the release activity and bioavailability of sEVs and MgBG. Additionally, it is essential to consider that wound healing is a complex process involving four continuous and overlapping stages, necessitating the effective function of sEVs and MgBG at all stages for optimal results.

In this study, a novel hydrogel dressing has been developed by combining sEVs with PPMB to form vesicle clusters, which were then incorporated into a hydrogel. This dressing, based on a comprehensive repair strategy, promoted angiogenesis in the immunoregulatory microenvironment throughout the four stages of wound healing. Initially, during the early treatment of hard-to-heal wounds, the EPPMO hydrogel dressing exhibited injectability, self-healing, and interfacial adhesion properties (Fig. 2d–f). The hydrogel dressing filled and adhered to irregular skin defects, forming a protective barrier to cover the wound and providing necessary healing conditions for DWs [47]. Under 808 nm NIR, the photoresponsive dressing (Fig. 2g–j) rapidly increased the ambient temperature to 45 °C, causing bacterial lysis and achieving a sterilization rate of over 99 % in a short period (Fig. 5), preventing a prolonged inflammatory environment caused by bacterial infection. In contrast, the blank group showed significant purulence from a macroscopic skin perspective due to the lack of bactericidal effect (Fig. 9b). Although the non-photoresponsive OQ and EO groups also demonstrated some bactericidal effects due to the positive charge of QCS, their sterilization was not as thorough as that of the photoresponsive hydrogel.

During the hemostasis and inflammation stages, the dressing has continuously released EPPM in response to pH changes. This process recruits L929s to the wound site and induces the polarization of macrophages towards the M2 phenotype, thereby establishing an anti-inflammatory microenvironment. While the EO and PPMO hydrogels also have some immunomodulatory capabilities (Fig. 7), the quantity and efficiency of sEVs and PPMB internalized by cells were relatively low (Fig. 4). In contrast, the vesicle clusters rich in sEVs released by EPPMO hydrogel were efficiently internalized by cells. The synergistic effect of miRNAs (e.g., miR146a) within sEVs and Mg^{2+} from MgBG rapidly promoted the polarization of macrophages to M2, inhibited TNF-α release, and enhanced IL-10 expression, exerting anti-inflammatory effects (Fig. 10a). During the proliferation stage, the hydrogel treatment system released EPPM vesicle clusters, which upregulated the expression of angiogenesis-related genes such as VEGF (Fig. 8), promoting angiogenesis (Fig. 10b), accelerating blood vessel formation, and restoring blood perfusion to the wound site. Additionally, MgBG and sEVs modulated macrophage release of factors such as IL-8 and CCL5 to recruit cells and accelerate tissue regeneration [9]. This was achieved through the efficient cellular uptake of the slow-released EPPM vesicle clusters rich in sEVs. During the remodeling stage, although the EO and PPMO hydrogel groups promoted some degree of epithelialization, the EPPMO hydrogel group exhibited significant skin appendages such as hair follicles and sebaceous glands, as well as mature collagen deposition, indicating high-quality healing of the skin (Figs. S10 and 10c).

Consistent with in vitro results, in vivo macroscopic observation and histological analysis have confirmed the anti-inflammatory and photothermal antibacterial effects of sEVs and PPMB in chronic wound healing. Thus, the combination of EPPMO and NIR irradiation has developed a promising platform for accelerating diabetic wound healing, with advantages including antibacterial activity, inflammation inhibition, and angiogenesis promotion. These results in vivo evaluation suggested that the EPPMO hydrogel doped with EPPM offered great potential for future clinical applications in chronic wounds for diabetic patients.

3. Conclusion

In summary, a novel concept has been demonstrated by programming stem cell-derived sEVs through functionalized MgBG interfaces to create vesicle clusters (EPPM) that are efficiently endocytosed by functional cells involved in wound healing (macrophages, HUVECs). This approach, combined with injectable, self-healing, and bioadhesive hydrogels, has led to the development of a comprehensive repair system (EPPMO) that promotes healing throughout the inflammatory and proliferative stages of diabetic wound healing. PDA and PLL-modified MgBG has enabled effective self-assembly programming of sEVs, and exhibited high photothermal conversion efficiency, providing excellent photothermal antibacterial performance under NIR irradiation without compromising sEVs activity. Furthermore, cell experiments have confirmed that the EPPMO dressing released EPPM vesicle clusters, which were efficiently endocytosed by wound healing-related functional cells (including endothelial cells and macrophages), thereby demonstrating the synergistic anti-inflammatory and pro-angiogenic capabilities of sEVs and MgBG. In addition, in vivo experiments have validated the therapeutic efficacy of EPPMO in promoting wound closure in STZ-induced diabetic rats. Overall, this comprehensive repair system has shown significant antibacterial, anti-inflammatory, cell migration-promoting, angiogenesis-enhancing, and vesicle delivery-enhancing capabilities, making it a promising candidate for diabetic wound healing applications.

4. Materials and methods

4.1. Materials

Dodecylamine (DDA), Tetraethyl Orthosilicate (TEOS), Triethyl Phosphate (TEP), Calcium Nitrate Tetrahydrate (CN), Magnesium Nitrate (MN, Aladdin, China), Dopamine (DA, Aladdin, China), Poly-L-lysine (PLL), Sodium Periodate ($NaIO_4$, Aladdin, China), LB agar (Aladdin, China) were provided from Shanghai Aladdin Biochemical Technology Co., Ltd (Shanghai, China). Dextran, Chitosan (CS), Glycidyl Trimethylammonium Chloride (GTMAC), FITC were obtained from Sigma-Aldrich (Shanghai) Trading Co.,Ltd. Dio, 4 % paraformaldehyde, 0.1 % crystal violet were obtained from Shanghai Beyotime Biotechnology Co.,Ltd.

4.2. Preparation and physicochemical characterization of PPMB

The preparation of MgBG was based on a previously established method by our research group [44]. Briefly, 4 g of dodecylamine (DDA, Aladdin, China) was dissolved in a mixture of 80 mL anhydrous ethanol and 25 mL deionized water (DIW) at 40 °C. Subsequently, 16 mL of tetraethyl orthosilicate (TEOS, Aladdin, China) was added dropwise, and the mixture was stirred for 30 min. Every 30 min, 1.66 mL of triethyl phosphate (TEP, Aladdin, China), 8.837 g of calcium nitrate tetrahydrate (CN, Aladdin, China), and 1.547 g of magnesium nitrate (MN, Aladdin, China) were sequentially added. The mixture was stirred at 40 °C for 3 h. The crude product was obtained by centrifugation and washed three times with anhydrous ethanol and DIW. Finally, the crude

product was sintered in air at 650 °C for 3 h to obtain the final MgBG product.

The preparation of PPMB involved dispersing 1 g of MgBG in 100 mL of Tris-HCl (pH = 8.5) solution and subjecting the mixture to ultrasonic treatment for 30 min. Subsequently, 0.1 g of dopamine (DA, Aladdin, China) was added to the MgBG dispersion and stirred at room temperature for 24 h with the container open. Next, 0 g, 0.02 g, and 0.05 g of PLL (Aladdin, China) were measured and added to the mixture, which was stirred for an additional 24 h. The mixture was then centrifuged at 5000×*g* for 10 min, washed three times with deionized water, and dried at 60 °C to obtain three types of nanoparticles: PDA-MgBG, PP0.2-MB, and PP0.5-MB.

The particle size and zeta potential of the nanoparticles were measured using a particle size analyzer (Zetasizer Nano ZSE, Malvern, USA). The microstructure and elemental composition were analyzed using SEM (Zeiss, Germany) and XRD (Empyrean, Netherlands).

4.3. Synthesis and characterization of OD and QCS

Synthesis of OD [48]: 10 g of dextran (Sigma-Aldrich, USA) was dissolved in 150 mL of DIW and stirred at room temperature for 3 h in the dark. A 1:1 ratio of 10 mL sodium periodate ($NaIO_4$, Aladdin, China) was slowly added, and the mixture was stirred at room temperature for 4 h to partially oxidize the dextran. The reaction was terminated by adding 2 mL of glycerol. The product was dialyzed in a dialysis bag (2k-4k Da) for 3 d, with the water changed every 12 h. The OD product was obtained by freeze-drying the dialyzed solution.

Synthesis of QCS [20]: 3 g of CS (Sigma-Aldrich, USA) was mixed with 90 mL of DIW and 0.5 % (v/v) glacial acetic acid, and stirred at room temperature for 30 min. GTMAC (Sigma-Aldrich, USA) was dissolved in 18 mL of DIW in a molar ratio of 2:1 (GTMAC, structural units) and stirred at 55 °C for 18 h. After the reaction, the mixture was centrifuged at 4500 rpm for 30 min to remove impurities. The supernatant was gently stirred into pre-cooled acetone at −20 °C for crude purification. The precipitate was redissolved, dialyzed in a dialysis bag (8k-14k Da) for 5 d with water changes every 12 h, and the QCS was obtained by freeze-drying. Characterization of OD and QCS was conducted by using FTIR (Fourier Transform Infrared Spectroscopy, Bruker, Germany)

4.4. Preparation and characterization of PPMO hydrogels

To prepare PPMO hydrogels, a QCS (2 %) solution A and an OD (4 %) gelatin solution B were first prepared. Solutions A and B were mixed in a 1:1 vol ratio. PP0.5-MB was added to solution B at total weight percentages of 0 %, 1.5 %, 3 %, and 5 % (w/v). The mixtures were then subjected to ultrasound treatment at 37 °C for 30 min. The resulting hydrogels were designated as OQ, 1.5 % PPMO, 3 % PPMO, and 5 % PPMO, respectively.

To assess the injectability of PPMO hydrogel, red dye was added to the PPMO hydrogel. A 2 mL sample of the red PPMO hydrogel was placed into a 1 mL syringe and injected into star-shaped and circular molds. After demolding, photographs were taken to observe the injectability. Additionally, to evaluate the self-healing properties, the PPMO hydrogel was divided into red A hydrogel and blue B hydrogel. Both were shaped into rectangles and then cut in half with a scalpel. The cut surfaces of A and B hydrogels were then brought into contact for 2 min to observe the self-healing. Furthermore, to test interfacial adhesion, the red PPMO hydrogel was adhered to pig skin. The adhesion was observed by bending and folding the pig skin and by attempting to peel the hydrogel off the skin with tweezers. Photographs were taken to document the adhesive performance. Observation of the internal structure of the hydrogels was conducted using SEM.

To evaluate the interfacial adhesion of OQ, 1.5 % PPMO, 3 % PPMO, and 5 % PPMO hydrogels, fresh pig skin was purchased from the market and cleaned of excess fat for lap shear tests. The pig skin was cut into rectangles measuring 2 cm in length and 1 cm in width. A 100 μL volume of each hydrogel was applied to one piece of pig skin (A), which was then covered with another piece of pig skin (B) to create a contact area of 1 cm^2. The samples were kept hydrated by placing their bases in a small amount of PBS and were analyzed using dynamic thermomechanical analysis (DMA, Q800DE, USA) to assess their properties.

4.5. Photothermal responsiveness of PPMO hydrogels

To evaluate the photothermal properties of PPMO hydrogels, 200 μL of each hydrogel was placed at the bottom of a 24-well plates. The hydrogels were irradiated with 808 nm NIR at intensities of 0.5, 1, 1.5, and 2 W/cm^2. The results were observed using a NIR imaging system (FOTRIC 220s, America) and analyzed with the system's software.

4.6. Preparation and characterization of EPPM

This study employed differential centrifugation to isolate sEVs [48, 49]. BMSCs (2×10^6 cells, CRL-12424, ATCC, USA) were incubated in FBS-free DMEM (5 mL) for 48 h. The resulting medium underwent successive centrifugations at 2000×*g* and 10,000×*g* for 30 min each to remove larger particles. The supernatant was then centrifuged at 100, 000×*g* for 70 min to pellet the sEVs. These sEVs were resuspended in PBS, washed twice, and filtered through a 0.22 μm sterile filter. The protein concentration was measured using the BCA Protein Assay Kit (Solarbio, China). TEM (HT7700, HITACHI, Japan) was used to visualize the morphology. Zeta potential analysis (Malvern, America) potential and determined particle size distribution. The presence of specific proteins (CD9, CD63, calnexin, TSG101, Bioss) was confirmed by Western blotting.

The preparation of EPPM involved measuring 2 mg each of MgBG, PDA-MgBG, PP0.2-MB, and PP0.5-MB, followed by adding 1 mL of PBS solution and subjecting the mixture to ultrasonic treatment for 30 min. MgBG was mixed with sEVs at a mass ratio of 10:1 (MgBG). The mixture was stirred slowly in an ice bath for 2 h and then centrifuged at 5000×*g* for 15 min. The supernatant was collected to obtain the composite nanoparticles: sEVs@MgBG, sEVs@PDA-MgBG, sEVs@PP0.2-MB, and sEVs@PP0.5-MB. The remaining concentration of sEVs in the supernatant was measured using a BCA protein assay kit, and the loading rate of sEVs was calculated. According to the manufacturer's instructions, sEVs were labeled with Dio (Beyotime, China), a green fluorescent cell membrane marker. Images were captured and assessed using LSCM (TCS SP8, Leica, Germany).

To assess the distribution of sEVs@PPMB in the hydrogel, 10 mg of PP0.5-MB has been immersed in FITC (Sigma-Aldrich, USA) solution (1 mg/mL) and stirred at room temperature for 24 h to obtain FITC-labeled PP0.5-MB. Separately, sEVs have been labeled using the Dil staining kit (Beyotime, China). The labeled PP0.5-MB and sEVs have been combined to prepare EPPMO hydrogel, and their distribution has been observed and analyzed using LSCM.

To evaluate the release performance of sEVs from EO hydrogel and EPPMO hydrogel, these hydrogels were immersed in PBS solutions with pH = 7.4 and 6.5. Samples of PBS were collected at specific time points to measure the release amount of sEVs.

4.7. In vitro antibacterial properties of EPPMO hydrogels

To evaluate the photothermal antibacterial performance of EPPMO hydrogel, preliminary antibacterial experiments were conducted. Initially, 16 g of LB agar (Aladdin, China) was dissolved in 0.5 L of DIW and sterilized by autoclaving. When the LB agar solution cooled to 60–70 °C, it was poured into petri dishes at 20 mL per dish and allowed to cool overnight under ventilation to obtain sterile agar plates. Separately, 12 g of broth was dissolved in 0.5 L of DIW and sterilized by autoclaving to obtain sterile broth solution.

200 μL of hydrogel was placed at the bottom of each well in 24-well

plates. Each well was inoculated with 20 μL of broth solution containing *S. aureus* or *E. coli* at a concentration of 7×10^8 CFU/mL. The hydrogels were divided into two groups: NIR (+), subjected to 808 nm NIR irradiation at 1 W/cm^2 for 6 min, and NIR (−), without NIR treatment. All hydrogels were incubated at 37 °C with 5 % CO_2 for 2 h. Subsequently, 980 μL of broth was added to each well and mixed thoroughly. 10 μL was spread on agar plates, which were incubated overnight at 37 °C with 5 % CO_2. Bacterial growth was photographed and analyzed.

Additionally, 10 μL of the bactericidal broth was added to 15 mL centrifuge tubes, diluted with 980 μL of broth, and incubated overnight at 37 °C with 5 % CO_2. After thorough mixing, 150 μL was transferred to 96-well plates, and absorbance at 600 nm was measured using a microplate reader. The bactericidal rate of EPPMO hydrogel was calculated using the formula:

$$\text{Bactericidal Rate} = (W0 - Wt)/W0 \times 100\ \%$$

Where *W0* was the absorbance of the Control group (untreated bacteria), and *Wt* was the absorbance of the experimental group.

4.8. Biocompatibility and recruit ability testing of EPPMO hydrogels

To evaluate the impact of EPPMO hydrogel on the viability of L929s (TCM-C749, HyCyte, China) and HUVECs (DFSC-EC-01, Shanghai Zhong Qiao Xin Zhou Biotechnology Co.,Ltd, China), the CCK8 assay was utilized. Initially, L929s and HUVECs were seeded in 24-well plates at a density of 2×10^4 cells/well and cultured for 24 h. Subsequently, 50 μL of sterile hydrogel was added to the upper chamber of Transwell inserts and co-cultured with L929s for 1, 3, and 7 d. The CCK8 assay (Beyotime, China) was performed according to the manufacturer's instructions. Cells were incubated with the CCK8 working solution for 2 h, and the absorbance at 450 nm was measured using a microplate reader.

Live/Dead staining was conducted by diluting Calcein AM/propidium iodide (Beyotime, China) according to the manufacturer's instructions and incubating with the cells for 30 min. Images have been acquired and analyzed by using LSCM.

Hemocompatibility test of the hydrogels was conducted. In brief, red blood cells (RBCs) were collected by centrifuging the whole sheep blood at 1200 rpm for 10 min, and then diluted the obtained RBCs tenfold (v/v) with PBS. Each component of hydrogel was added to 2 mL of whole blood at a ratio of 200 mg/mL, and equal volumes of Triton-X 100 and PBS were also added as positive and negative controls. All components was incubated at room temperature for 1 h and centrifuged at 3000 rpm for 10 min. The hemocompatibility of each group was observed. 100 μL of supernatant was transferred to 96-well plates and measured the absorbance at 540 nm wavelength using a microplate reader. The hemolysis rate was calculated according to the following formula:

$$\text{Hemolysis Ratio} = \frac{OD\ (sample)\text{-}OD\ (negative)}{OD\ (positive)\text{-}OD\ (negative)} \times 100\%$$

To assess the hydrogel's ability to recruit L929s, a Transwell migration assay was performed. L929s were seeded in the upper chamber of Transwell inserts at a density of 2×10^4 cells/well, and 50 μL of sterile hydrogel was added to the lower chamber, followed by a 12 h incubation. Cells were fixed with 4 % paraformaldehyde (Beyotime, China) for 30 min and stained with 0.1 % crystal violet (Beyotime, China) for 30 min. Images were captured using an inverted microscope and analyzed with Image J software.

The scratch assay was used to evaluate the migration ability of L929s. L929s were seeded in 24-well plates at a density of 2×10^4 cells/well and cultured for 24 h. A vertical scratch was created using a 200 μL sterile pipette tip. Additionally, 50 μL of sterile hydrogel was added to the upper chamber of Transwell inserts. After a 24 h co-culture with L929s, images were captured using an inverted microscope and analyzed with Image J software. The cell migration rate wasn't calculated using the formula:

$$\text{Cell migration rate} = (M0 - Mt)/M0 \times 100\ \%$$

Where *M*0 was the initial scratch area at 0 h, and *M*t is the scratch area at 24 h.

4.9. Anti-inflammation detection of EPPMO hydrogel

To evaluate the capacity of hydrogel adjuncts in modulating inflammation-related gene expression, reverse transcription quantitative polymerase chain reaction (RT-qPCR) was utilized to assess the expression of anti-inflammatory genes. RAW 264.7 cells (TIB-71, ATCC, USA) were seeded at a density of 2×10^4 cells/well in the bottom of a 24-well plates and cultured for 24 h. Subsequently, the medium was replaced with complete medium containing LPS (Beyotime, China) at a concentration of 100 ng/mL, and the cells were cultured for an additional 8 h. Following this, 50 μL of sterile EPPMO hydrogels was added to the upper chamber of Transwell inserts. Co-culturing continued for 3 d to facilitate RT-qPCR experiments for gene expression analysis.

Total RNA was extracted using the Total RNA Kit I (Omega, America) and converted into cDNA using a reverse transcription kit (Takara, Japan). RT-qPCR was performed using the LightCycler 480 SYBR Green I Master (Roche, Switzerland) and analyzed on the LightCycler® 480II system (Roche, Switzerland). Quantification was performed using the $2^{-\Delta\Delta Ct}$ method. The primer sequences for each gene were provided in Table S2.

Furthermore, intracellular expressions of p65, iNOS, and IL-10 proteins were analyzed by immunofluorescence. Cells were fixed by incubating with 4 % paraformaldehyde for 20 min, followed by permeabilization of cell membranes with 0.2 % Triton X-100 (BioFroxx, Germany) for 10 min and blocking with 3 % goat serum for 30 min. Primary antibodies (p65, iNOS, IL-10, Bioss, China) were applied and incubated overnight at 4 °C, followed by incubation with secondary antibodies in the dark at room temperature for 2 h. Finally, nuclei were stained with DAPI (Beyotime, China) for 5 min. Images were captured and analyzed by using LSCM.

4.10. Angiogenic properties of EPPMO hydrogel

RT-qPCR was employed to assess the expression of angiogenesis-related genes in HUVECs treated with hydrogel. HUVECs were seeded at a density of 3×10^4 cells/well in 24-well plates and cultured for 24 h. Sterile hydrogel (50 μL) was added to the upper chamber of a Transwell and co-cultured with HUVECs for 3 and 7 d. RT-qPCR was used to detect angiogenesis-related gene expression, and immunofluorescence was used to detect CD31 (Bioss, China) expression. The detection method was described in Section 3.8. The primer sequences were provided in Table S2. Vasculogenesis was investigated by culturing HUVECs on 96-well plates coated matrigel (Beyotime, China) for 8 h, and analyzed by calcein AM staining.

4.11. Animal experimentation

To evaluate the hydrogel's ability to promote skin repair, a full-thickness skin defect model of diabetic infected wounds in SD rats was used. All animal procedures were performed in accordance with the Guidelines for Care and Use of Laboratory Animals of Guangzhou seyotin Biotechnology Co., LTD and approved by the Animal Ethics Committee of Guangzhou seyotin Biotechnology Co., LTD. (SYT2024041), selecting male SD rats aged 8 weeks and weighing 200–250 g. Initially, a type 1 diabetes model was established by collecting blood from the tail end of the rats and measuring and recording their blood glucose levels. An intraperitoneal injection of streptozotocin (STZ, Solarbio, China) at a dose of 70 mg/kg (1 % concentration) was administered. After 48 h, blood glucose levels were measured using a glucometer. Fasting blood glucose levels greater than or equal to 11.1 mmol/L or non-fasting blood glucose levels greater than 16.7 mmol/L

indicate successful induction of diabetes in the rats.

One day following the successful establishment of the diabetic rat model, the skin injury model was initiated. The rats were anesthetized, placed on a surgical table in the prone position, and their back hair shaved to fully expose the dorsal skin. After routine surgical disinfection, a full-thickness skin area of 1 cm in diameter was excised from the back of each rat. A circular ring with an inner diameter of 10 mm, an outer diameter of 12 mm, and a thickness of 1 mm was sutured around the wound, with four stitches placed at the diagonal positions of the circle. S. aureus (20 μL, 7×10^8 CFU/mL) was added, followed by 200 μL of hydrogel in the experimental groups. NIR irradiation (1 W/cm^2) was applied for 6 min. Samples were collected on days 3, 7, and 14. Wound photographs were taken to calculate the healing rate, with the wound area assessed using area measurement software. The wound closure rate was calculated as follows:

$$\text{Wound closure rate} = (T0 - Tn) / T0 \times 100\ \%$$

Where $T0$ represented the wound area on day 0, and Tn represented the wound area on day n (n = 3, 7, or 14).

To further analyze the therapeutic effects of the hydrogel, tissues were transferred to 4 % paraformaldehyde for 72 h and subsequently subjected to decalcification, embedding, and sectioning. Subsequently, tissue sections were stained with H&E, Masson's trichrome, and immunofluorescence stains. Images were captured and analyzed using a digital pathology scanning system.

4.12. Statistical analysis

Using SPSS 22.0 statistical analysis software, a one-way analysis of variance followed by Tukey's test for means comparison was used to assess the level of significance.

CRediT authorship contribution statement

Zetao Wang: Writing – original draft, Methodology, Investigation, Data curation. **Zhipeng Sun:** Writing – original draft, Software, Formal analysis, Data curation. **Shuangli Zhu:** Software, Resources, Methodology, Conceptualization. **Zhihao Qin:** Validation, Software, Methodology. **Xiaohong Yin:** Resources, Methodology, Formal analysis. **Yilin Ding:** Resources, Methodology, Investigation. **Huichang Gao:** Writing – review & editing, Methodology, Formal analysis. **Xiaodong Cao:** Supervision, Project administration, Funding acquisition, Conceptualization.

Ethics approval and consent to participate

All animal procedures were performed in accordance with the Guidelines for Care and Use of Laboratory Animals of Guangzhou seyotin Biotechnology Co., LTD and approved by the Animal Ethics Committee of Guangzhou seyotin Biotechnology Co., LTD. (SYT2024041)

Declaration of competing interest

The authors declare that they have no known competing financial interests or personal relationships that could have appeared to influence the work reported in this paper.

Acknowledgments

This work was supported by the National Natural Science Foundation of China (Grant No. 52272276, 52073103, 52203164), the Fundamental Research Funds for the Central Universities (No. 2022ZYGXZR105), the Project funded by China Postdoctoral Science Foundation (No. 2022M711183), the Science and Technology Planning Project of Guangzhou (2023A04J0971).

Appendix A. Supplementary data

Supplementary data to this article can be found online at https://doi.org/10.1016/j.bioactmat.2025.03.025.

References

[1] N. Singh, D.G. Armstrong, B.A. Lipsky, Preventing foot ulcers in patients with diabetes, JAMA 293 (2) (2005) 217–228. https://10.1001/jama.293.2.217.
[2] V. Falanga, Wound healing and its impairment in the diabetic foot, Lancet 366 (9498) (2005) 1736–1743. https://10.1016/S0140-6736(05)67700-8.
[3] Y. Guan, H. Niu, Z. Liu, Y. Dang, J. Shen, M. Zayed, L. Ma, J. Guan, Sustained oxygenation accelerates diabetic wound healing by promoting epithelialization and angiogenesis and decreasing inflammation, Sci. Adv. 7 (35) (2021). https://10.1126/sciadv.abj0153.
[4] J.C. Brazil, M. Quiros, A. Nusrat, C.A. Parkos, Innate immune cell-epithelial crosstalk during wound repair, J. Clin. Investig. 129 (8) (2019) 2983–2993. https://10.1172/jci124618.
[5] Y. Xiong, B.B. Mi, Z. Lin, Y.Q. Hu, L. Yu, K.K. Zha, A.C. Panayi, T. Yu, L. Chen, Z. P. Liu, A. Patel, Q. Feng, S.H. Zhou, G.H. Liu, The role of the immune microenvironment in bone, cartilage, and soft tissue regeneration: from mechanism to therapeutic opportunity, Mil Med Res 9 (1) (2022) 65. https://10.1186/s40779-022-00426-8.
[6] Y.F. Zheng, X.N. Gu, F. Witte, Biodegradable metals, Mater. Sci. Eng. R Rep. 77 (2014) 1–34. https://10.1016/j.mser.2014.01.001.
[7] X.Y. Wang, W.J. Zheng, Z.Z. Bai, S. Huang, K. Jiang, H.M. Liu, L. Liu, Mimicking bone matrix through coaxial electrospinning of core-shell nanofibrous scaffold for improving neurogenesis bone regeneration, Biomater. Adv. 145 (2023). https://10.1016/j.bioadv.2022.213246.
[8] W. Qiao, K.H.M. Wong, J. Shen, W. Wang, J. Wu, J. Li, Z. Lin, Z. Chen, J. P. Matinlinna, Y. Zheng, S. Wu, X. Liu, K.P. Lai, Z. Chen, Y.W. Lam, K.M.C. Cheung, K.W.K. Yeung, TRPM7 kinase-mediated immunomodulation in macrophage plays a central role in magnesium ion-induced bone regeneration, Nat. Commun. 12 (1) (2021) 2885. https://10.1038/s41467-021-23005-2.
[9] Y. Xiong, Z. Lin, P.Z. Bu, T. Yu, Y. Endo, W. Zhou, Y. Sun, F.Q. Cao, G.D. Dai, Y. Q. Hu, L. Lu, L. Chen, P. Cheng, K.K. Zha, M.A. Shahbazi, Q. Feng, B.B. Mi, G. H. Liu, A whole-course-repair system based on neurogenesis-angiogenesis crosstalk and macrophage reprogramming promotes diabetic wound healing, Adv. Mater. 35 (19) (2023). https://10.1002/adma.202212300.
[10] Y. Kang, C. Xu, L. Meng, X.F. Dong, M. Qi, D.Q. Jiang, Exosome-functionalized magnesium-organic framework-based scaffolds with osteogenic, angiogenic and anti-inflammatory properties for accelerated bone regeneration, Bioact. Mater. 18 (2022) 26–41. https://10.1016/j.bioactmat.2022.02.012.
[11] R. Tejido-Rastrilla, S. Ferraris, W.H. Goldmann, A. Grünewald, R. Detsch, G. Baldi, S. Spriano, A.R. Boccaccini, Studies on cell compatibility, antibacterial behavior, and zeta potential of Ag-containing polydopamine-coated bioactive glass-ceramic, Materials 12 (3) (2019) 13. https://10.3390/ma12030500.
[12] H. Ma, Q. Zhou, J. Chang, C. Wu, Grape seed-inspired smart hydrogel scaffolds for melanoma therapy and wound healing, ACS Nano 13 (4) (2019) 4302–4311. https://10.1021/acsnano.8b09496.
[13] S. Zhang, S.J. Chuah, R.C. Lai, J.H.P. Hui, S.K. Lim, W.S. Toh, MSC exosomes mediate cartilage repair by enhancing proliferation, attenuating apoptosis and modulating immune reactivity, Biomaterials 156 (2018) 16–27. https://10.1016/j.biomaterials.2017.11.028.
[14] X. Zhou, Z.Y. Wang, Y.K. Chan, Y.M. Yang, Z. Jiao, L.M. Li, J.Y. Li, K.N. Liang, Y. Deng, Infection micromilieu-activated nanocatalytic membrane for orchestrating rapid sterilization and stalled chronic wound regeneration, Adv. Funct. Mater. 32 (7) (2022) 23. https://10.1002/adfm.202109469.
[15] J.H. Ch'ng, K.K.L. Chong, L.N. Lam, J.J. Wong, K.A. Kline, Biofilm-associated infection by enterococci, Nat. Rev. Microbiol. 17 (2) (2019) 82–94. https://10.1038/s41579-018-0107-z.
[16] Y.P. Liang, M. Li, Y.T. Yang, L.P. Qiao, H.R. Xu, B.L. Guo, pH/glucose dual responsive metformin release hydrogel dressings with adhesion and self-healing via dual-dynamic bonding for athletic diabetic foot wound healing, ACS Nano 16 (2) (2022) 3194–3207. https://10.1021/acsnano.1c11040.
[17] Y.Q. Zhao, Y. Sun, Y. Zhang, X. Ding, N. Zhao, B. Yu, H. Zhao, S. Duan, F.J. Xu, Well-defined gold nanorod/polymer hybrid coating with inherent antifouling and photothermal bactericidal properties for treating an infected hernia, ACS Nano 14 (2) (2020) 2265–2275. https://10.1021/acsnano.9b09282.
[18] W.I. Choi, A. Sahu, Y.H. Kim, G. Tae, Photothermal cancer therapy and imaging based on gold nanorods, Ann. Biomed. Eng. 40 (2) (2012) 534–546. https://10.1007/s10439-011-0388-0.
[19] S.L. Zhu, Q.Y. Dai, L.T. Yao, Z.T. Wang, Z.C. He, M.C. Li, H. Wang, Q.T. Li, H. C. Gao, X.D. Cao, Engineered multifunctional nanocomposite hydrogel dressing to promote vascularization and anti-inflammation by sustained releasing of Mg2+ for diabetic wounds, Compos. Pt. B-Eng. 231 (2022) 16. https://10.1016/j.compositesb.2021.109569.
[20] Y. Huang, L. Mu, X. Zhao, Y. Han, B.L. Guo, Bacterial growth-induced tobramycin smart release self-healing hydrogel for Pseudomonas aeruginosa-infected burn wound healing, ACS Nano 16 (8) (2022) 13022–13036. https://10.1021/acsnano.2c05557.

[21] J. Qu, X. Zhao, Y.P. Liang, T.L. Zhang, P.X. Ma, B.L. Guo, Antibacterial adhesive injectable hydrogels with rapid self-healing, extensibility and compressibility as wound dressing for joints skin wound healing, Biomaterials 183 (2018) 185–199. https://10.1016/j.biomaterials.2018.08.044.
[22] J.C. Tang, K. Xi, H. Chen, L.J. Wang, D.Y. Li, Y. Xu, T.W. Xin, L. Wu, Y.D. Zhou, J. Bian, Z.W. Cai, H.L. Yang, L.F. Deng, Y. Gu, W.G. Cui, L. Chen, Flexible osteogenic glue as an all-in-one solution to assist fracture fixation and healing, Adv. Funct. Mater. 31 (38) (2021) 16. https://10.1002/adfm.202102465.
[23] Y. Li, R.Z. Fu, Z.G. Duan, C.H. Zhu, D.D. Fan, Artificial nonenzymatic antioxidant MXene nanosheet-anchored injectable hydrogel as a mild photothermal-controlled oxygen release platform for diabetic wound healing, ACS Nano 16 (5) (2022) 7486–7502. https://10.1021/acsnano.1c10575.
[24] S. Zhu, M. Li, Z. Wang, Q. Feng, H. Gao, Q. Li, X. Chen, X. Cao, Bioactive glasses-based nanozymes composite macroporous cryogel with antioxidative, antibacterial, and pro-healing properties for diabetic infected wound repair, Adv. Healthcare Mater. 12 (29) (2023) e2302073. https://10.1002/adhm.202302073.
[25] W.C. Li, S.J. Wu, L. Ren, B.Y. Feng, Z.P. Chen, Z.T. Li, B. Cheng, J. Xia, Development of an antiswelling hydrogel system incorporating M2-exosomes and photothermal effect for diabetic wound healing, ACS Nano 17 (21) (2023) 22106–22120. https://10.1021/acsnano.3c09220.
[26] R. Kalluri, V.S. LeBleu, The biology, function, and biomedical applications of exosomes, Science 367 (6478) (2020) 640. https://10.1126/science.aau6977.
[27] X.C. Du, B.Q. Jia, W.J. Wang, C.M. Zhang, X.D. Liu, Y.Y. Qu, M.W. Zhao, W.F. Li, Y. M. Yang, Y.Q. Li, pH-switchable nanozyme cascade catalysis: a strategy for spatial-temporal modulation of pathological wound microenvironment to rescue stalled healing in diabetic ulcer, J. Nanobiotechnol. 20 (1) (2022) 16. https://10.1186/s12951-021-01215-6.
[28] Y.P. Liang, X. Zhao, P.X. Ma, B.L. Guo, Y.P. Du, X.Z. Han, pH-responsive injectable hydrogels with mucosal adhesiveness based on chitosan-grafted-dihydrocaffeic acid and oxidized pullulan for localized drug delivery, J. Colloid Interface Sci. 536 (2019) 224–234. https://10.1016/j.jcis.2018.10.056.
[29] Y.N. Zhu, J.M. Zhang, J.Y. Song, J. Yang, Z. Du, W.Q. Zhao, H.S. Guo, C.Y. Wen, Q. S. Li, X.J. Sui, L. Zhang, A multifunctional pro-healing zwitterionic hydrogel for simultaneous optical monitoring of pH and glucose in diabetic wound treatment, Adv. Funct. Mater. 30 (6) (2020). https://10.1002/adfm.201905493.
[30] N. Jin, Z.L. Wang, X. Tang, N.Q. Jin, X.H. Wang, Promoting diabetic wound healing through a hydrogel-based cascade regulation strategy of fibroblast-macrophage, Adv. Healthcare Mater. (2024). https://10.1002/adhm.202400526.
[31] X. Zhao, Y.P. Liang, Y. Huang, J.H. He, Y. Han, B.L. Guo, Physical double-network hydrogel adhesives with rapid shape adaptability, fast self-healing, antioxidant and NIR/pH stimulus-responsiveness for multidrug-resistant bacterial infection and removable wound dressing, Adv. Funct. Mater. 30 (17) (2020). https://10.1002/adfm.201910748.
[32] S. Tomar, R. Pandey, P. Surya, R. Verma, R. Mathur, G. Gangenahalli, S. Singh, Multifunctional, adhesive, and PDA-coated bioactive glass reinforced composite hydrogel for regenerative wound healing, ACS Biomater. Sci. Eng. 9 (3) (2023) 1520–1540. https://10.1021/acsbiomaterials.2c01223.
[33] H. Min, J. Wang, Y.Q. Qi, Y.L. Zhang, X.X. Han, Y. Xu, J.C. Xu, Y. Li, L. Chen, K. M. Cheng, G.N. Liu, N. Yang, Y.Y. Li, G.J. Nie, Biomimetic metal-organic framework nanoparticles for cooperative combination of antiangiogenesis and photodynamic therapy for enhanced efficacy, Adv. Mater. 31 (15) (2019). https://10.1002/adma.201808200.
[34] D. Pamu, V. Tallapaneni, V. Karri, S.K. Singh, Biomedical applications of electrospun nanofibers in the management of diabetic wounds, Drug Delivery and Translational Research 12 (1) (2022) 158–166. https://10.1007/s13346-021-00941-6.
[35] L.I.F. Moura, A.M.A. Dias, E. Carvalho, H.C. de Sousa, Recent advances on the development of wound dressings for diabetic foot ulcer treatment-A review, Acta Biomater. 9 (7) (2013) 7093–7114. https://10.1016/j.actbio.2013.03.033.
[36] J.Y. Wu, L.L. Chen, R.F. Wang, Z. Song, Z.S. Shen, Y.M. Zhao, S. Huang, Z.M. Lin, Exosomes secreted by stem cells from human exfoliated deciduous teeth promote alveolar bone defect repair through the regulation of angiogenesis and osteogenesis, ACS Biomater. Sci. Eng. 5 (7) (2019) 3561–3571. https://10.1021/acsbiomaterials.9b00607.
[37] C.N. Lumeng, J.L. Bodzin, A.R. Saltiel, Obesity induces a phenotypic switch in adipose tissue macrophage polarization, J. Clin. Investig. 117 (1) (2007) 175–184. https://10.1172/jci29881.
[38] J. Zheng, R. Fan, H.Q. Wu, H.H. Yao, Y.J. Yan, J.M. Liu, L. Ran, Z.F. Sun, L.Z. Yi, L. Dang, P.P. Gan, P. Zheng, T.L. Yang, Y. Zhang, T. Tang, Y. Wang, Directed self-assembly of herbal small molecules into sustained release hydrogels for treating neural inflammation, Nat. Commun. 10 (2019). https://10.1038/s41467-019-09601-3.
[39] L. Fan, P.F. Guan, C.R. Xiao, H.Q. Wen, Q.Y. Wang, C. Liu, Y.A. Luo, L.M. Ma, G. X. Tan, P. Yu, L. Zhou, C.Y. Ning, Exosome-functionalized polyetheretherketone-based implant with immunomodulatory property for enhancing osseointegration, Bioact. Mater. 6 (9) (2021) 2754–2766. https://10.1016/j.bioactmat.2021.02.005.
[40] Z.J. Lin, D.N. Shen, W.X. Zhou, Y.F. Zheng, T.T. Kong, X.Y. Liu, S.L. Wu, P.K. Chu, Y. Zhao, J. Wu, K.M.C. Cheung, K.W.K. Yeung, Regulation of extracellular bioactive cations in bone tissue microenvironment induces favorable osteoimmune conditions to accelerate in situ bone regeneration, Bioact, Mater. 6 (8) (2021) 2315–2330. https://10.1016/j.bioactmat.2021.01.018.
[41] M. Wang, C.G. Wang, M. Chen, Y.W. Xi, W. Cheng, C. Mao, T.Z. Xu, X.X. Zhang, C. Lin, W.Y. Gao, Y. Guo, B. Lei, Efficient angiogenesis-based diabetic wound healing/skin reconstruction through bioactive antibacterial adhesive ultraviolet shielding nanodressing with exosome release, ACS Nano 13 (9) (2019) 10279–10293. https://10.1021/acsnano.9b03656.
[42] Y.P. Liang, X. Zhao, T.L. Hu, B.J. Chen, Z.H. Yin, P.X. Ma, B.L. Guo, Adhesive hemostatic conducting injectable composite hydrogels with sustained drug release and photothermal antibacterial activity to promote full-thickness skin regeneration during wound healing, Small 15 (12) (2019). https://10.1002/smll.201900046.
[43] L. Liu, F. Yu, L. Li, L.X. Zhou, T. Zhou, Y.J. Xu, K.L. Lin, B. Fang, L.G. Xia, Bone marrow stromal cells stimulated by strontium-substituted calcium silicate ceramics: release of exosomal miR-146a regulates osteogenesis and angiogenesis, Acta Biomater. 119 (2021) 444–457. https://10.1016/j.actbio.2020.10.038.
[44] S.L. Zhu, Q.Y. Dai, L.T. Yao, Z.T. Wang, Z.C. He, M.C. Li, H. Wang, Q.T. Li, H. C. Gao, X.D. Cao, Engineered multifunctional nanocomposite hydrogel dressing to promote vascularization and anti-inflammation by sustained releasing of Mg^{2+} for diabetic wounds, Compos. Pt. B-Eng. 231 (2022). https://10.1016/j.compositesb.2021.109569.
[45] J.H. Lee, J.J. Kwak, H.B. Shin, H.W. Jung, Y.K. Lee, E.D. Yeo, S.S. Yang, Comparative efficacy of silver-containing dressing materials for treating MRSA-infected wounds in rats with streptozotocin-induced diabetes, Wounds-a Compendium of Clinical Research and Practice 25 (12) (2013) 345–354.
[46] H.W. Li, X. Chen, K. Ren, L.H. Wu, G. Chen, L. Xu, Qualitative study on diabetic cutaneous wound healing with radiation crosslinked bilayer collagen scaffold in rat model, Sci. Rep. 13 (1) (2023). https://10.1038/s41598-023-33372-z.
[47] Y.P. Liang, J.H. He, B.L. Guo, Functional hydrogels as wound dressing to enhance wound healing, ACS Nano 15 (8) (2021) 12687–12722. https://10.1021/acsnano.1c04206.
[48] Z.T. Wang, H.F. Li, H.T. Luo, H. Wang, Z.M. Ling, D.F. Chen, Q. Feng, X.D. Cao, Extracellular vesicles loaded dual-network bioactive sealant via immunoregulation and annulus fibrosus repair for intervertebral disc herniation, J. Mater. Sci. Technol. 184 (2024) 75–87. https://10.1016/j.jmst.2023.10.034.
[49] Z.T. Wang, H.T. Luo, Z.Y. Zhou, Z.Y. He, S.L. Zhu, D.G. Li, H.C. Gao, X.D. Cao, Engineered multifunctional Silk fibroin cryogel loaded with exosomes to promote the regeneration of annulus fibrosus, Appl. Mater. Today 29 (2022). https://10.1016/j.apmt.2022.101632.